

# Unveiling Multiple Physical Processes on a Cluster Galaxy at $z = 0.3$ Using JWST

Peter J. Watson<sup>1</sup>, Benedetta Vulcani<sup>1</sup>, Ariel Werle<sup>1</sup>, Bianca Poggianti<sup>1</sup>, Marco Gullieuszik<sup>1</sup>, Michele Trenti<sup>2,3</sup>, Xin Wang<sup>4,5,6</sup>, and Namrata Roy<sup>7</sup>

<sup>1</sup> INAF – Osservatorio Astronomico di Padova, Vicolo Osservatorio 5, 35122 Padova, Italy

e-mail: peter.watson@inaf.it

<sup>2</sup> School of Physics, University of Melbourne, Parkville, Vic 3010, Australia

<sup>3</sup> Australian Research Council Centre of Excellence for All-Sky Astrophysics in 3-Dimensions, Australia

<sup>4</sup> School of Astronomy and Space Science, University of Chinese Academy of Sciences (UCAS), Beijing 100049, China

<sup>5</sup> National Astronomical Observatories, Chinese Academy of Sciences, Beijing 100101, China

<sup>6</sup> Institute for Frontiers in Astronomy and Astrophysics, Beijing Normal University, Beijing 102206, China

<sup>7</sup> Center for Astrophysical Sciences, William H. Miller III Department of Physics and Astronomy, Johns Hopkins University, Baltimore, MD, 21218

Received September 15, 1996; accepted March 16, 1997

## ABSTRACT

We present a study of a previously identified candidate “jellyfish” galaxy in the Abell 2744 cluster, F0083, which showed faint signs of a tidal interaction in archival imaging. We used publicly available, PSF-matched deep photometric data from the Hubble and James Webb Space Telescopes, to infer the spatially-resolved star-formation history of this galaxy. F0083 shows clear signs of ram-pressure stripping (RPS), with a recently enhanced star-formation rate (SFR) orientated towards the South-West quadrant of the stellar disc. The stellar mass surface density is heavily asymmetric, with a variation of nearly 1 dex between the Western spiral arm and the postulated tidal feature. This feature appears to contain a high proportion of older stars, ruling out RPS as the cause of this “unwinding”. An investigation of nearby galaxies reveals the most probable interaction candidate to be a compact elliptical galaxy, 28171, of mass  $\log_{10}(M_*/M_\odot) = 8.53 \pm 0.04$ , embedded in the tidal stream along our line-of-sight. The star-formation history of the tidal feature indicates a steep change in SFR at lookback times  $t_L \lesssim 1$  Gyr. The most probable formation scenario of F0083 thus indicates a low-speed interaction with 28171, followed by RPS as the combined system approaches pericentre passage. Our results demonstrate the ability of photometric data to distinguish between these consecutive processes.

**Key words.** galaxies: clusters: individual: A2744 – galaxies: interactions – galaxies: evolution – galaxies: stellar content

## 1. Introduction

It has long been known that one of the primary driving forces in galaxy evolution is the surrounding environment (Oemler 1974; Dressler 1980; Larson et al. 1980; Cortese et al. 2021). Compared to their counterparts in the field, galaxies within dense environments such as clusters have substantially different properties on average, often appearing redder, and comprising a higher fraction of ellipticals and fewer spirals (Dressler 1980). Whilst the more isolated field galaxies may only evolve through internal processes, the evolution of galaxies in clusters is heavily affected by external physical processes. These can be divided into two main subclasses: gravitational and hydrodynamical.

Gravitational processes include all interactions between galaxies, such as tidal interactions and galaxy harassment (Merritt 1983; Byrd & Valtonen 1990; Moore et al. 1996; Nulsen 1982). These processes can affect the distribution of stellar mass within a galaxy, leading to extended tidal streams containing older stars, as well as inducing spiral structure, either symmetric or asymmetric depending on the relative interaction velocity (Wei et al. 2021). They can disrupt the accretion and cooling of gas from the intergalactic medium (IGM), or compress the interstellar medium (ISM) in tidal features, leading to enhanced star-formation rates (SFR) (Renaud et al. 2014). By contrast, hy-

drodynamic processes encompass all interactions between the dense plasma within the cluster halo (the intracluster medium, or ICM), and the ISM of a galaxy moving at a range of velocities. These interactions include ram-pressure stripping (RPS; Gunn & Gott 1972; Takeda et al. 1984), thermal evaporation (Cowie & Songaila 1977), starvation (Larson et al. 1980; Balogh et al. 2000), and viscous stripping (Nulsen 1982). These processes, in contrast to the gravitational processes, are able to directly remove the gas from the galaxy without affecting the existing stellar content, usually resulting in a rapid cessation of star formation.

Ram-pressure stripping stands out amongst the hydrodynamical processes. Whilst it is one of the most efficient methods of removing gas, depending on the orientation and relative velocity of the host galaxy (Akerman et al. 2023), it does not initially prevent star formation. Due to the progression of the galaxy through the cluster medium, the stripped gas can be observed in various phases as a “tail”. This gas cools into star-forming knots, leading to extended tails that are visible across almost the entire electromagnetic spectrum, from X-ray to radio continuum (e.g. Wang et al. 2004; Sun et al. 2010; Gullieuszik et al. 2023; Moretti et al. 2022; Gavazzi et al. 1995; Scott et al. 2012; Roberts et al. 2021; Serra et al. 2024). The most spectacular examples of

RPS are known as “jellyfish” galaxies, so named for the peculiar morphology of these knots and filaments trailing the stellar disc (Smith et al. 2010; Poggianti et al. 2017).

Due to the variety of interplaying physical processes, it remains difficult to obtain a full understanding of galactic evolution within high-density environments. Some observations indicate that RPS is almost ubiquitous amongst blue galaxies in relatively local clusters (Boselli et al. 2018; Vulcani et al. 2022), and that the fraction observed is simply an artefact of the duration of visibility of the tails compared to the total duration of stripping. On the other hand, galaxy mergers and other low-velocity interactions are thought to be rare in high-mass clusters, due to the high velocity dispersion of the system, with repeated high-velocity encounters favoured (harassment Moore et al. 1996).

There are scant few galaxies in which both processes have been observed. Serra et al. (2024), investigating the HI distribution of NGC 1427A ( $z_{\text{spec}} = 0.007$ ), conclude that its properties cannot be explained by RPS alone, and are suggestive of a previous high-speed merger. Similarly, using the Multi-Unit Spectroscopic Explorer (MUSE), Fritz et al. (2017) detail the jellyfish galaxy JO36 ( $z_{\text{spec}} = 0.041$ ), which appears to have been partially stripped by interactions with the ICM, before a gravitational interaction distorted the remaining gas and stellar disc. Looking at non-cluster environments, Vulcani et al. (2021) find only a single galaxy in which multiple processes can be identified using MUSE, from a sample of 27 asymmetric field galaxies. The interaction between these gravitational and hydrodynamical processes is thus almost completely unexplored, particularly at earlier epochs. We aim to demonstrate that by using multi-band photometry to derive spatially-resolved star formation histories, it is possible to isolate both the location and duration of these processes.

### 1.1. Abell 2744

The target environment for this study is the Abell 2744 galaxy cluster, hereinafter A2744 (R.A. = 3.58641, Dec. =  $-30.39997$ ,  $z_{\text{spec}} = 0.3064$ ). This is an extremely well-observed system, albeit a highly complex environment, giving rise to the nickname “Pandora’s Cluster” (Merten et al. 2011). It has long been known to have significant merger activity, based on the identification of an extended radio halo and radio relic (Giovannini et al. 1999; Govoni et al. 2001a,b). More recent observations have identified at least four radio relics in the vicinity of the cluster, up to 1 Mpc away from the centre (Pearce et al. 2017; Rajpurohit et al. 2021; Golovich et al. 2019), and X-ray data indicate multiple peaks, shock fronts, and cold fronts (Kempner & David 2004; Owers et al. 2011; Merten et al. 2011; Jauzac et al. 2016; Chadayammuri et al. 2024). The cluster itself contains no less than four interacting subclusters, with some disagreement on the precise location, mass, and membership of these structures, depending on whether they are derived from velocity distributions (Boschin et al. 2006; Rawle et al. 2014; Vulcani et al. 2023) or gravitational lensing maps (Merten et al. 2011; Medezinski et al. 2016; Kokorev et al. 2022; Bergamini et al. 2023; Cha et al. 2024).

The dynamical state and multiple components of A2744 make it extremely difficult to find any consensus on its formation history. Thus far, the two most robust claims are that one merger has occurred near the plane of the sky, in the North-South direction, and that another has occurred in the South-East of the cluster, with a large line-of-sight velocity component. Whilst there are additional hypotheses relating to substructures in the West or North-West of the cluster (Kempner & David 2004; Merten

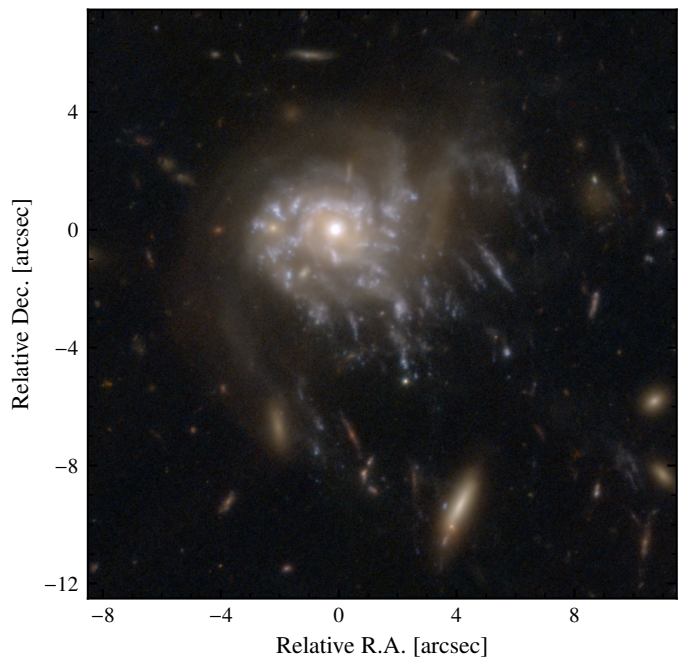


**Fig. 1.** A colour image of the galaxy F0083, created by combining publicly available imaging from the Hubble and James Webb Space Telescopes (HST and JWST) at their native resolution, in the following bands: F435W, F606W, F070W, F814W, F090W, F115W, F150W, and F200W.

et al. 2011; Medezinski et al. 2016), these are not relevant to our analysis, and are not considered further.

The N-S merger is often referred to using the substructure nomenclature of Owers et al. (2011), as the Northern (Major Remnant) Core (NC) and the Central Tidal Debris (CTD). The third major substructure, the Southern Minor Remnant Core (SMRC), has a projection coincident with the Central Tidal Debris, but is offset in velocity space by  $\sim 5000 \text{ km s}^{-1}$ , and may not even be gravitationally bound to the remainder of the cluster (Chadayammuri et al. 2024). These names, however, may be misleading. More recent analyses converge on a scenario where the majority of mass is contained within the Southern core of the cluster, the CTD, and both the NC and SMRC have passed through this region within the last Gyr (Mahler et al. 2018; Furtak et al. 2023; Bergamini et al. 2023; Cha et al. 2024).

### 1.2. The Target: F0083

The main subject of this paper is a large ( $\approx 12'' \times 12''$ , or  $55 \times 55 \text{ kpc}$ ) spiral galaxy, shown in colour in Fig. 1. It is located on the South-Eastern side of Abell 2744 (R.A. = 3.61066, Dec. =  $-30.39560$ ), at a redshift  $z = 0.3033$ , and is consistent with being a member of either the CTD substructure, or the general cluster environment. This unique galaxy, hereinafter referred to as F0083 after Owers et al. (2012), has previously been identified as a potential “jellyfish”, or ram-pressure stripped galaxy, with a possible tidal feature (see Section 1.3 for a comprehensive overview of the published literature). However, the studies thus far have not conclusively established that either of these mechanisms affect F0083, and whether there are any alternative explanations for its formation and evolution.

For example, there are many instances of more local galaxies with highly disturbed morphologies and elevated star-formation rates, resulting from mergers rather than interactions within a

cluster environment (the Whirlpool, Antennae, and Mice galaxies being amongst the most well-known). Whilst F0083 is located within the cluster, it is possible that interactions with other galaxies have dominated the history of this object, resulting in the observed morphology. On the other hand, it has recently been suggested that one of the effects of ram-pressure stripping may be to “unwind” the spiral arms of galaxies, due to the differential pressure exerted as a result of the disc rotation (Bellhouse et al. 2017, 2021; Vulcani et al. 2022). These different mechanisms should each leave a distinctive mark on the star-formation history (SFH) of the galaxy (and any interacting neighbours), and it is this that we aim to exploit, through spatially-resolved SED fitting to deep photometric observations.

### 1.3. Previous Studies

F0083 has been observed previously, in a small number of studies, and we discuss these briefly below. The first is Owers et al. (2012), from which we adopt their assigned name, who identified this object as a potential jellyfish galaxy using HST/ACS imaging in the F435W, F606W, and F814W bands. They identified the presence of a low-luminosity active galactic nucleus (AGN,  $L_X \sim 10^{41}$  erg s $^{-1}$ ) based on Chandra X-ray observations of the cluster field, and through double Gaussian fits to single fibre spectroscopy on the galaxy centre, using AAOmega on the Anglo-Australian Telescope (Owers et al. 2011). Intriguingly, they also suggested the presence of a tidal feature, connecting to a faint galaxy on the eastern side, indicating an interaction. However, due to the data available at the time, it was not possible to comment further on this.

Rawle et al. (2014) investigated a number of galaxies in the A2744 field, amongst them F0083. Using GALEX NUV and SPITZER/IRAC observations, they estimated the UV and IR SFRs as  $SFR_{UV} = 26.2 \pm 0.9 M_{\odot} \text{ yr}^{-1}$  and  $SFR_{IR} = 8.0 \pm 1.0 M_{\odot} \text{ yr}^{-1}$  respectively, accounting for the AGN luminosity in the IR regime. From the  $SFR_{UV}/SFR_{IR}$  ratio, they suggested that F0083 is likely starbursting, and has been observed near peak star formation efficiency as the dusty gas reservoir has been almost completely exhausted. They also estimated the total stellar mass using IRAC 3.6 and 4.5  $\mu\text{m}$  fluxes, using the relation from Eskew et al. (2012), giving a result of  $\log_{10}(M_*/M_{\odot}) \approx 10.91$ , for a Kroupa (2001) initial mass function (IMF). Rawle et al. (2014) also posited that an infall scenario was unlikely for this galaxy, as the orientation of the visible blue tail is not aligned to the radial line of the cluster core, and that it had been stripped due to shock fronts from mergers of the cluster cores themselves – although there is no clear consensus on the formation history of the cluster (Merten et al. 2011; Golovich et al. 2019; Rajpurohit et al. 2021; Cha et al. 2024).

Most recently, Lee et al. (2022a) and Lee et al. (2022b) observed F0083 in part with the GMOS IFU, over the range 7820–9260  $\text{\AA}$ . Whilst this only covered a limited field of view ( $5'' \times 7''$ ) encompassing the central component and a portion of the blue tail, they estimated a total  $SFR = 22.0 M_{\odot} \text{ yr}^{-1}$  in the region they observed (accounting for AGN emission), with  $\approx 35\%$  of star formation occurring in the tail. However, it is worth noting that the  $H\alpha$ -derived SFRs from Lee et al. (2022b) trace more recent star formation than either the  $SFR_{UV}$  or  $SFR_{IR}$  used by Rawle et al. (2014), and are not directly comparable. They highlight that the galaxy shows clear signs of a rotating gas disc, and that the  $H\alpha$  flux contours are highly asymmetric, being extended towards the eastern region.

### 1.4. Aims and Hypothesis

The central hypothesis of this paper is that F0083 represents a rare example of a galaxy undergoing ram-pressure stripping, following an interaction with a nearby galaxy producing a tidal stream. In Section 2 we present the data and the methods utilised to extract the necessary measurements, showing these results for F0083 in Section 3. In Section 4 we discuss and interpret these results, comparing them against the existing literature and simulations. We also identify nearby galaxies that may have interacted, and contrast their derived star-formation histories against F0083. Finally, in Section 5, we summarise the salient points of this work, and discuss the implications and potential for further study. Throughout this paper, we assume a Kroupa (2001) IMF, and a solar metallicity  $Z_{\odot} = 0.0142$  (Asplund et al. 2009). Coordinates are given in the International Celestial Reference System (ICRS), and we assume a standard  $\Lambda$  cold dark matter cosmology, with  $\Omega_M = 0.3$ ,  $\Omega_{\Lambda} = 0.7$ , and  $h = 0.7$ .

## 2. Method

Whilst F0083 is the primary target, we do also consider other nearby galaxies. The data and methods detailed here apply to all such galaxies throughout this study.

### 2.1. Available Data

The data used in this study comprise all publicly available imaging using NIRCcam and NIRISS on JWST, as well as WFC3/UVIS, WFC3/IR, and ACS/WFC on HST. The main contributions to the JWST imaging are GLASS-JWST ERS (Treu et al. 2022; Paris et al. 2023; Merlin et al. 2024), UNCOVER (Bezanson et al. 2022; Weaver et al. 2024), and MegaScience (Suess et al. 2024), with a full list of all contributing programmes in Appendix A. We use here the drizzled mosaics made public through the most recent MegaScience data release (Suess et al. 2024)<sup>1</sup>, which combine all of these existing observations. The mosaics were reduced using the “jwst\_0995.pmap” calibration reference file, and aligned and co-added using the Grism Redshift & Line pipeline (GRIZLI, Brammer 2019). All mosaics are normalised to have flux intensity units of  $10 \text{ nJy pix}^{-1}$ , corresponding to an AB magnitude zeropoint of 28.9, and are sampled onto a grid with a scale of 0.04'' per pixel. At the redshift of the A2744 cluster ( $z = 0.3064$ ), this corresponds to a physical scale of 4.52 kpc per pixel.

### 2.2. PSF Matching

For accurate spatially-resolved photometry, it is necessary to ensure that all measurements are made on images with a similar point-spread function (PSF). Given the large variation in the size and shape of the PSF, from the UVIS filters on HST/WFC3 to the long-wavelength (LW) filters on JWST/NIRCcam, this requires deriving convolution kernels to match a target PSF. For simplicity, we follow the lead of Suess et al. (2024), and match to the NIRCcam F444W filter. The MegaScience public data release includes empirical PSFs and convolution kernels for 27 of the 33 filters with coverage in the regions of interest. We therefore use these PSFs and kernels where available, and derive our own PSFs for the remaining filters, with the procedure detailed in Appendix B.

<sup>1</sup> These data releases are presently available at <https://jwst-uncover.github.io/DR3.html>

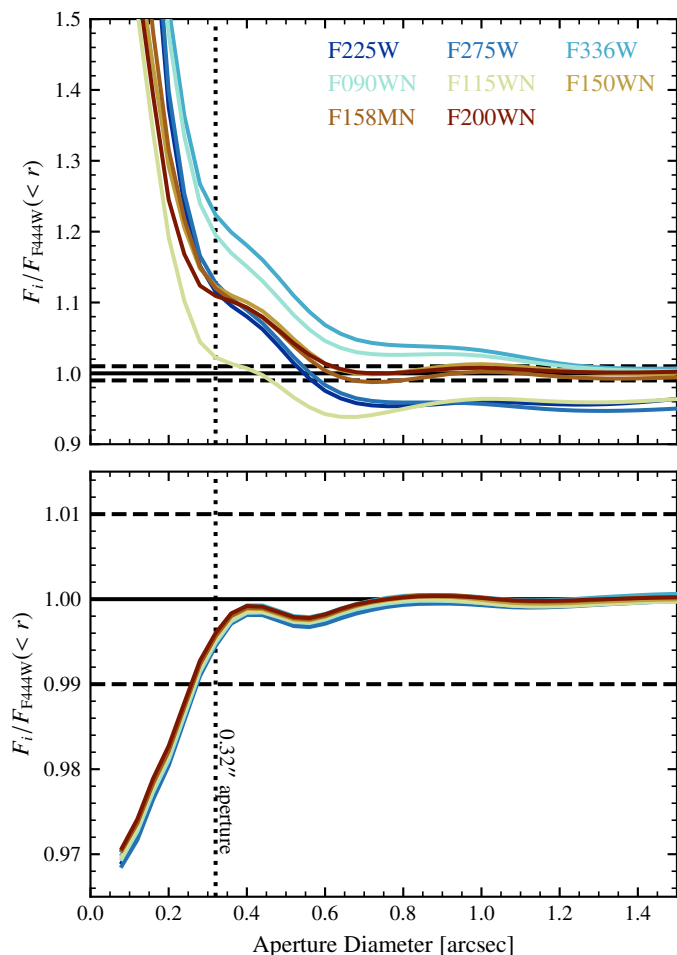


**Fig. 2.** The PSF curve of growth for each filter in our analysis, before (top) and after (bottom) matching to the F444W PSF. The curves are shown as the encircled flux relative to the F444W growth curve, where unity would imply an exact match. The solid black line indicates an exact match, the dashed lines the  $\pm 1\%$  deviations from this, and the dotted line the location of a  $0.32''$  aperture, for ease of comparison with the growth curves shown in Weaver et al. (2024) and Suess et al. (2024).

In Fig. 2, we compare the encircled energy of our matched PSFs against the target, as a function of the aperture diameter. Comparing against the results shown in Fig. 6 of Weaver et al. (2024) and Fig. 3 of Suess et al. (2024), our results are of a similar quality to the existing PSF-matching kernels. The maximum deviation from the target PSF is  $\approx 3\%$ , at an aperture diameter of  $0.06''$  (1.5 pixels), consistent with the residual pattern shown in Fig. B.1e. Some variation is unavoidable, given the vastly different shape and substructure of the PSFs, but we highlight that at apertures larger than  $\approx 0.27''$ , the encircled flux in all filters is consistent within 1% of the F444W target.

### 2.3. Voronoi Binning

To maintain a sufficient signal/noise (S/N) when deriving the spatially-resolved properties, it is necessary to bin the data in some form. For our science case, we aim to satisfy two criteria:

- The S/N in each bin must be sufficient to reliably constrain the SFH, given the non-parametric form detailed in Section 2.5.
- The bin size must be large enough to avoid sampling at scales where the PSF convolution is highly uncertain.

On the latter point, we require a minimum bin radius of  $0.27''$ , as this is the minimum diameter for which the encircled energy of every matched PSF deviates by less than 1% from the target (see Section 2.2). We therefore adopt a modified version of the Weighted Voronoi Tessellation technique, developed by Cappellari & Copin (2003) and Diehl & Statler (2006), in which bin shapes tend towards close-packed hexagons. Consequently, during the initial step of the algorithm, we restrict the progression such that a new bin cannot be initiated until the current bin has accreted at least 30 pixels, the area corresponding to a hexagon with circumcircular diameter  $0.27''$ . To calculate the S/N, we use the flux in the NIRCcam F150W filter as the signal, and for the noise the square root of the full variance array in the same filter, including contributions from the read noise, sky background, and the Poisson noise from individual sources.

### 2.4. Redshifts

Throughout this paper, for cluster galaxies other than F0083 we make use of redshifts from the MegaScience data release catalogue (Suess et al. 2024). These photometric redshifts,  $z_{\text{phot}}$ , were derived through SED fitting to the integrated flux in all available photometric bands, using the SED fitting tool PROSPECTOR (Johnson et al. 2021), and the physical model of Wang et al. (2024). We refer the reader to the aforementioned papers for further details. For a small number of galaxies in the A2744 field, there exist spectroscopic redshifts,  $z_{\text{spec}}$ . We cross-matched the locations of galaxies in the MegaScience catalogue against the spectroscopic catalogue compiled by Bergamini et al. (2023), and the NIRSpc catalogue of Mascia et al. (2024). Where available, we make use of these measurements instead of the maximum-likelihood photometric redshifts.

### 2.5. SED Fitting

We model the stellar populations of each galaxy by fitting the observed fluxes in all photometric bands with the SED fitting code, BAGPIPES (Bayesian Analysis of Galaxies for Physical Inference and Parameter ESTimation, Carnall et al. 2018). For Voronoi-binned galaxies, the fluxes in each band are measured as the sum of the fluxes of all pixels within each Voronoi bin. The uncertainties are measured similarly, albeit with an additional 5% uncertainty term added in quadrature to account for systematic effects (see Appendix C). BAGPIPES uses the Bruzual & Charlot (2003) spectral library<sup>2</sup>, updated with the 2016 version of the MILES library of empirical spectra (Falc3n-Barroso et al. 2011).

We adopt a non-parametric form for the SFH, following the method of Leja et al. (2019). We fit for a constant SFR in multiple bins of the lookback time  $t_L$ , where the bin edges are set at 0, 0.02, 0.05, 0.1, 0.25, 0.5, 1, 2, 5, 7.5, and 10 Gyr. The exact edge of the final bin is determined by the age of the universe at the redshift of the fitted galaxy, *i.e.*  $\approx 10$  Gyr for F0083 at  $z = 0.3033$ . Dust attenuation is described by the Milky Way extinction curve of Cardelli et al. (1989), with  $R_V = 3.1$ . We allow for the attenuation  $A_V$  to vary between zero and two magnitudes, and for  $\eta$ , the multiplicative factor on  $A_V$  for stars in birth clouds, to vary as  $0.5 \leq \eta \leq 3$ , both with uniform priors. Emission lines and nebular continuum emission are included in the fit for stellar populations as old as 20 Myr, via a method based on Byler et al. (2017), using the CLOUDY photoionisation code (Ferland et al. 2017). The ionisation parameter  $\log U$  is allowed to

<sup>2</sup> [https://www.bruzual.org/~gbruzual/bc03/Updated\\_version\\_2016/](https://www.bruzual.org/~gbruzual/bc03/Updated_version_2016/)

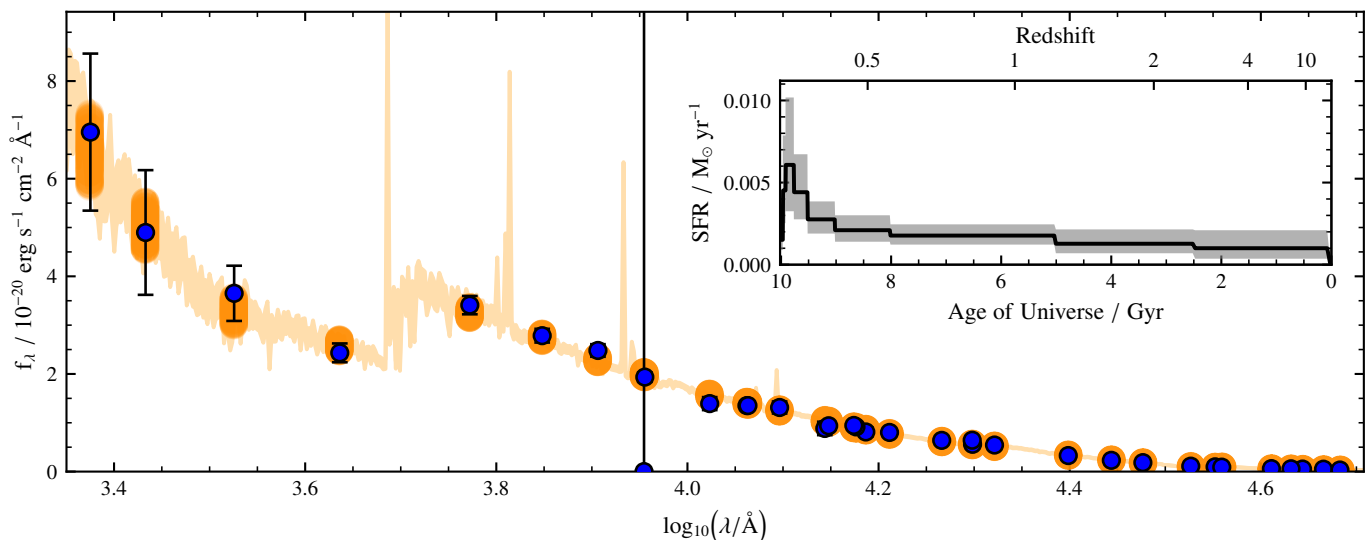


**Fig. 3.** An example BAGPIPES fit to the photometry in a single Voronoi bin. The blue points indicate the measured flux at the pivot point of each filter, with their uncertainty (including the additional systematic component). The shaded orange region indicates the 16<sup>th</sup>-84<sup>th</sup> percentile of the model spectrum, and the orange points the corresponding predicted fluxes in each filter. Inset, we show the derived star-formation history of this region as a function of both redshift and the age of the universe, with the shaded region denoting the 16<sup>th</sup>-84<sup>th</sup> percentile of the posterior PDF in each age bin.

vary between  $-3.5$  and  $-2$ . The stellar metallicity is assumed to be the same as the gas-phase metallicity, and is allowed to vary between  $0.01$  and  $2.5 Z_{\odot}$ , following a Gaussian prior with mean  $\mu = Z_{\odot}$  and standard deviation  $\sigma = 0.5 Z_{\odot}$ . The redshift is fixed to the galaxy redshift (see Section 2.4), as variations in velocity within a galaxy have a negligible effect on the broad-band photometry (Werle et al. 2024).

To sample the posterior distribution, BAGPIPES uses the MULTINEST nested sampling algorithm (Feroz et al. 2019), through the PYMULTINEST interface (Buchner et al. 2014). For our data, we run BAGPIPES with the default MULTINEST sampling parameters, using 400 live points. We show an example of the resulting photometric fit in Fig. 3. For bins in which the flux in one of the photometric bands is unusable (e.g. due to pixels masked during the mosaic creation), we set the flux to zero, and the uncertainty to  $10^{30}$ , which effectively discards that filter from the fit.

## 2.6. Contamination Masking

We define the extent of F0083 using SExtractor (Bertin & Arnouts 1996), by finding the connected region  $3\sigma$  above the local sky background, measured using a stack of the JWST/NIRCam imaging in the F115W, F150W and F200W filters. We opt to initially mask out the central seven bins for F0083, covering an approximate diameter of  $0.5''$ . The reasons for doing so are two-fold. Firstly, as F0083 hosts a low-luminosity AGN, there is a non-negligible contribution from this component to the photometry in bins near the centre of the galaxy. The spectral energy distribution of AGN can appear extremely similar to the continuum shape of young stellar populations, due to the underlying non-thermal emission, and it is not possible to break this degeneracy using only broad-band photometry. This can introduce significant biases in SED fitting codes such as BAGPIPES, leading to the inference of much younger and more massive stellar populations, than without the AGN contribution (Ciesla et al. 2015; Cardoso et al. 2017). Given the target F444W PSF, this masked region should contain  $> 85\%$  of

the point-source flux. We note, however, that the extended structure of the PSF (the so-called ‘‘snowflake’’ substructure, and the diffraction spikes) will still contribute a non-negligible amount of flux to the remainder of the bins (see Section 3.3, specifically Fig. 7). Whilst this artefact may have some small impact on our results, we do not consider it significant enough to affect the overall conclusions. The secondary factor is that the central pixels are saturated or show non-linear behaviour in a number of bands, notably the long-wavelength NIRCam bands, F277W, F356W, and F444W, in an aperture of  $\approx 0.25''$  diameter. These bands are vital for deriving accurate estimates of older stellar populations, and hence the total stellar mass. To avoid any potential bias in our conclusions, we prefer to mask this region entirely.

We also highlight that within the extent of F0083, the MegaScience data catalogue contains six other objects (see Fig. 1). Using the best-fit redshifts from Section 2.4, we discover that only one of these sources is within the approximate range of the cluster,  $0.29 \leq z \leq 0.32$  (see Section 4.1 for further details). Without dedicated spectroscopy, it is not possible to disentangle the flux contributed by any of these overlapping objects. Following our masking of the central AGN, we again opt for a conservative approach, and mask out the contaminated pixels (based on the SExtractor-derived segmentation map), visible in Fig. 4 as black regions. As a result of these masked areas, we stress that some of the integrated properties of our galaxy should be considered a slight underestimate of the true values, specifically the stellar mass and SFR.

## 3. Results

Whilst there are many derived quantities from our SED-fitting procedure, we focus here on the most relevant properties for our investigation that are well-constrained by the broad-band photometry. In particular, we look at the distribution of stellar mass and the SFR, both at the present epoch and as a function of look-back time  $t_L$ .

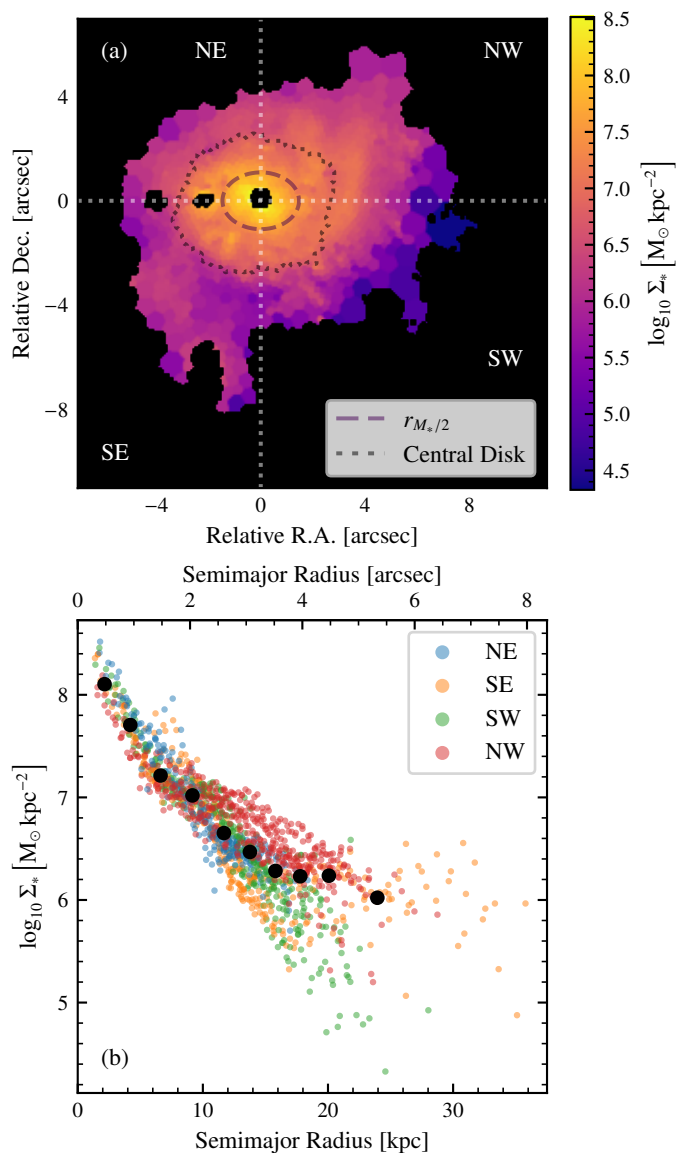


**Fig. 4.** (a) The spatially-resolved map of the stellar mass surface density for F0083, with all external objects masked out. We overlay the half-mass radius, and the contour we define as encompassing the central disc, in dashed and dotted lines respectively. (b) The radial profile of the stellar mass surface density, as a function of the semimajor axis length. Points are coloured according to the quadrant in which they lie. We also show the median profile, averaged in 10 radial bins.

### 3.1. Stellar Mass Distribution

From our BAGPIPES fits, we obtain an estimate of the current stellar mass in each Voronoi bin. Summing over all of the bins, we estimate the total stellar mass of F0083 to be  $\log_{10}(M_*/M_\odot) = 10.25 \pm 0.07$ . Compared against other studies such as Rawle et al. (2014), this appears substantially lower by  $\sim 0.6$  dex, although there are a number of contributing factors for this. Previous measures of the stellar mass have relied on the integrated flux in IRAC 3.6 and  $4.5 \mu\text{m}$  bands, using the relation of Eskew et al. (2012) to derive the stellar mass. However, in this study, they caution that the mass estimates are significantly affected by even a modest fraction of young stars in the population<sup>3</sup>, which it-

<sup>3</sup> An exact relation between the fraction of young stars and the estimated mass is not given, but the residuals are as high as 0.5 dex.

self is almost certainly large given the morphology and colour of F0083. Finally, in the same way that our measure is likely an underestimate due to our conservative masking procedure (see Section 2.6), it is highly likely that other measures overestimate the IR flux due to overlapping sources. Indeed, if we look at all bins for which the objects overlap in the original segmentation map, we instead find a mass of  $\log_{10}(M_*/M_\odot) = 10.41 \pm 0.1$ . As such, we do not consider this a significant discrepancy.

In Fig. 4a, we present the 2D map of the stellar mass surface density of F0083. We overlay the best-fit ellipse for the half-mass contour, enclosing half of the stellar mass, as a dashed line, giving a semimajor radius of  $r_{M_*/2} = 1.09 \pm 0.01''$  (or 4.89 kpc), ellipticity  $\epsilon = 0.26$ , and position angle  $\theta = 83.9$ . It is immediately clear that this galaxy has a disturbed morphology, with a significant degree of asymmetry in the mass distribution. In Fig. 4b, we highlight this by colouring the stellar mass surface density in each quadrant (with respect to the galaxy centre). Whilst we see a monotonic decrease for bins in the North-Eastern (NE) quadrant of F0083, there is a spike in stellar mass at a distance of  $\approx 8$  kpc in the SE quadrant. This corresponds to an extremely large star-forming region (see Section 3.2), visible in the direct imaging in Fig. 1. In the SW quadrant, the stellar mass density appears to flatten at large radii ( $> 15$  kpc), due to the recent star formation in the tail, whereas the NW region briefly plateaus between  $8 < r < 12$  kpc. This plateau is due to the presence of a large spiral arm, and there is little to no evidence for any equivalently massive structure on the opposing side, with an offset of  $\approx 0.5$  dex visible in Fig. 4b. There is however, a small increase in the mass surface density at an offset of  $\sim 5.5''$  from the centre towards the SE, in the location of the tidal feature reported by Owers et al. (2012). Whilst faint, this feature is also apparent as a yellow-red stream in the colour image in Fig. 1.

Many other studies of jellyfish galaxies use some estimate of the stellar disc, or the galaxy main body, as a point of comparison, derived through a variety of methods – e.g. manual masking (Lee et al. 2022b), *g*-band isophotes (Moretti et al. 2022), or the stellar continuum from spectral fitting (Gullieuszik et al. 2020). Here, we opt to derive an estimate from the F606W filter (the closest equivalent to rest-frame *g*). We adopt an ellipse with the same ellipticity and position angle as the half-mass contour (to prevent inclusion of the entire visible tail), and fit for the semimajor radius that matches the flux isophote  $5\sigma$  above the sky background. We refer to this as the “central disc”, and show its extent in Fig. 4. This allows us to compare the star formation histories in the exterior regions of F0083, whilst also providing a point of comparison to other studies. For reference, this region encompasses 81% of the total stellar mass of F0083 ( $\log_{10}(M_*/M_\odot) = 10.15$ , see Table 1).

### 3.2. Star Formation

The entire galaxy shows a considerable amount of ongoing star formation, albeit concentrated primarily within the centre, and towards the direction of the tail in the SW quadrant. In Fig. 5, we show the spatially-resolved specific star-formation rate (sSFR). The star-formation rate derived in BAGPIPES is averaged over the last 100 Myr, rather than the instantaneous measurement at time of observation (or the SFR in the most recent age bin), so it is most comparable to the SFR as traced by UV emission. As shown in Table 1, the integrated SFR over the full region of F0083 is  $20.8 \pm 2.6 M_\odot \text{yr}^{-1}$ , dropping to  $14.9 \pm 0.9 M_\odot \text{yr}^{-1}$  when the centre and other objects are masked. Whilst significantly lower than the  $\text{SFR}_{\text{UV}} = 26.2 \pm 0.9$  measured by Rawle et al. (2014), we note that whilst their study considered the AGN con-

**Table 1.** The properties of F0083 in different regions.

Region	$\log_{10}(M_*/M_\odot)$	$f_{M_*}$	$\text{Age}_{\text{MW}}$ [Gyr]	$\mu_{1.5}$	SFR [ $M_\odot \text{ yr}^{-1}$ ]	$f_{\text{SFR}}$	SFR <sub>20</sub> /SFR <sub>100</sub>
No Mask <sup>a</sup>	$10.33 \pm 0.07$	–	3.55	36%	$20.83 \pm 2.64$	–	1.37
Overlap Masked <sup>b</sup>	$10.30 \pm 0.07$	–	3.41	38%	$20.73 \pm 2.63$	– 1.37	
Centre Masked <sup>c</sup>	$10.25 \pm 0.07$	100.0%	3.35	38%	$14.94 \pm 0.87$	100.0%	1.17
Central disc <sup>d</sup>	$10.15 \pm 0.06$	80.0%	3.19	40%	$12.48 \pm 0.77$	83.5%	1.17
Exterior <sup>e</sup>	$9.55 \pm 0.07$	20.0%	4.00	30%	$2.46 \pm 0.10$	16.5%	1.13
A	$9.12 \pm 0.06$	7.4%	4.54	20%	$0.35 \pm 0.01$	2.3%	0.81
B	$8.77 \pm 0.07$	3.3%	3.56	35%	$0.20 \pm 0.01$	1.4%	0.89
C	$8.80 \pm 0.07$	3.6%	3.93	31%	$0.22 \pm 0.02$	1.4%	0.99
D	$8.25 \pm 0.07$	1.0%	2.25	59%	$0.14 \pm 0.01$	0.9%	0.90
E	$8.34 \pm 0.07$	1.2%	2.66	53%	$0.47 \pm 0.03$	3.1%	1.22
F	$8.79 \pm 0.08$	3.5%	4.16	34%	$1.09 \pm 0.08$	7.3%	1.30

**Notes.** The regions in this top panel of this table are defined as follows: <sup>(a)</sup> The entire connected region,  $3\sigma$  above the sky background. <sup>(b)</sup> All overlapping sources masked out. <sup>(c)</sup> As (b), but with the central seven bins masked out. <sup>(d)</sup> The area within the “central disc” contour (see Fig. 4a), with all masks applied. <sup>(e)</sup> The area outside the central disc, with all masks applied.

The regions in the bottom panel are those defined in Section 3.3. The fractional masses and star-formation rates,  $f_{M_*}$  and  $f_{\text{SFR}}$ , are defined relative to the “Centre Masked” region.

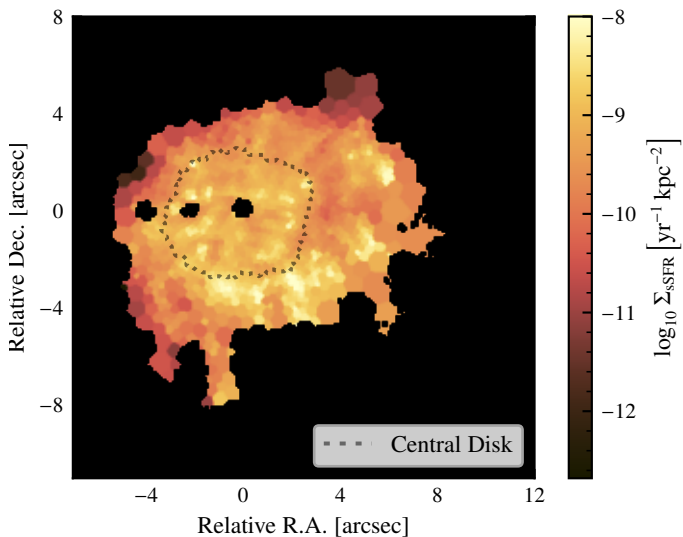


**Fig. 5.** The spatially-resolved map of the specific star-formation rate density for F0083. As in Fig. 4a, all external objects are masked out, and we display the central disc contour as a common point of reference.

tribution when deriving the SFR<sub>IR</sub>, they did not perform a similar analysis for SFR<sub>UV</sub>. As discussed in Section 2.6, this is therefore likely to be an overestimate of the UV contribution due to star formation alone. Likewise, our measurement underestimates the total SFR due to the conservative masking procedure, and the true value is likely between these two measurements.

### 3.3. Star Formation Histories

There are multiple methods in which to display and analyse the resolved star formation histories (SFH), and we focus here on two of the most pertinent. In Fig. 6, we decompose the exterior of F0083 (*i.e.* the area outside the central disc) into its constituent parts, based on a visual inspection of the colour image shown in Fig. 1, forming six regions. We distinguish between the two spiral arms (regions A and B), the putative tidal feature, and the blue knots and filaments comprising the tail. The tidal feature is further separated into an inner and outer component (regions C and D), following the discontinuity in the colour image, and

the tail divided into Eastern and Western regions (E and F), allowing for the possibility of different SFHs in the vicinity of the tidal feature. We then calculate the integrated properties of these regions, by combining the results from all Voronoi bins within the contour, with the results displayed in Table 1, and the SFHs in Fig. 6. We also calculate several additional quantities, used in previous studies (*e.g.* Werle et al. 2022) to compare the age and formation history of different stellar populations. These include  $\mu_{1.5}$ , the fraction of the stellar mass which formed within the last 1.5 Gyr,  $\text{Age}_{\text{MW}}$ , the mass-weighted age, and SFR<sub>20</sub>/SFR<sub>100</sub>, the ratio of the SFR over the last 20 Myr to the last 100 Myr, all of which are tabulated in Table 1.

We also look at the SFH of individual Voronoi bins. We integrate the SFR over a given temporal range to find the mass formed during that epoch, and compare this against the total mass formed since the beginning of the universe. The resulting maps of the mass fraction are shown in Fig. 7, with the previously defined regions overlaid as a consistent point of reference. We stress that there is a slight subtlety to these results. These maps represent the fraction of the stellar mass formed at a given epoch, within the *current* bin location, and should not be confused with the distribution of the stellar mass at earlier times. We summarise the salient points from these two figures below.

- Region A covers the majority of the North-Western spiral arm, containing  $\approx 7\%$  of the total stellar mass in F0083. By any measure, this is the oldest region, with  $\text{Age}_{\text{MW}} = 4.5$  Gyr, and  $\mu_{1.5} = 20\%$ . The inferred SFH in Fig. 6 shows a rising SFR until  $\approx 0.1$  Gyr ago, at which point it begins to decline. However, the overall variability in SFR is low, with  $\text{SFR}_{\text{max}}/\text{SFR}_{\text{min}} \approx 2$ . This is reflected in the fractional mass maps in Fig. 7, where the majority of the mass can be seen to have formed in the earliest time bins.
- Region B consists of the Northern spiral arm. Overall, this area appears to have formed more recently than region A, with a lower  $\text{Age}_{\text{MW}}$  and higher  $\mu_{1.5}$ , and a substantially lower SFR in the earliest age bins. Whilst this area has a currently declining SFR, it appears to peak  $\approx 500$  Gyr ago, with a sudden increase at  $t_L \approx 1$  Gyr.
- Region C covers the outermost part of the Eastern tidal feature. The shape of the SFH is extremely similar to region B, with a sudden increase in SFR at  $t_L \approx 1$  Gyr.

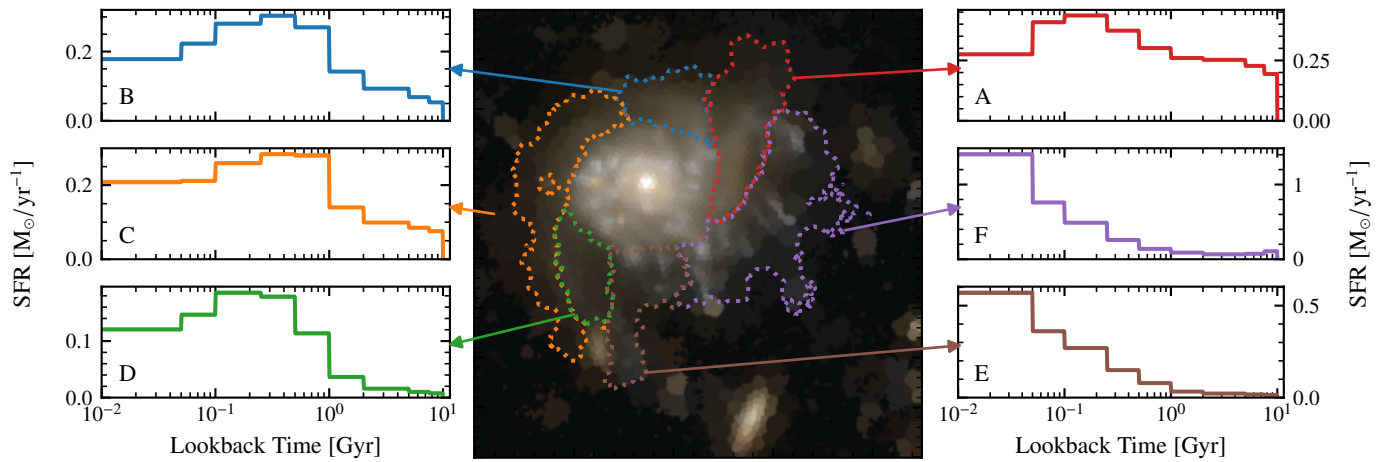


**Fig. 6.** (*centre*) An RGB image of F0083, using the same filters as in Fig. 1, constructed from the Voronoi-binned PSF-matched images. (*outsskirts*) The SFH in the exterior regions of the galaxy, summed over all bins in that region. The region label (A-F) is inset. Note that the SFR is plotted on a logarithmic scale, in contrast with Fig. 3, and hence the area under the line no longer directly represents the total stellar mass formed in a given temporal range.

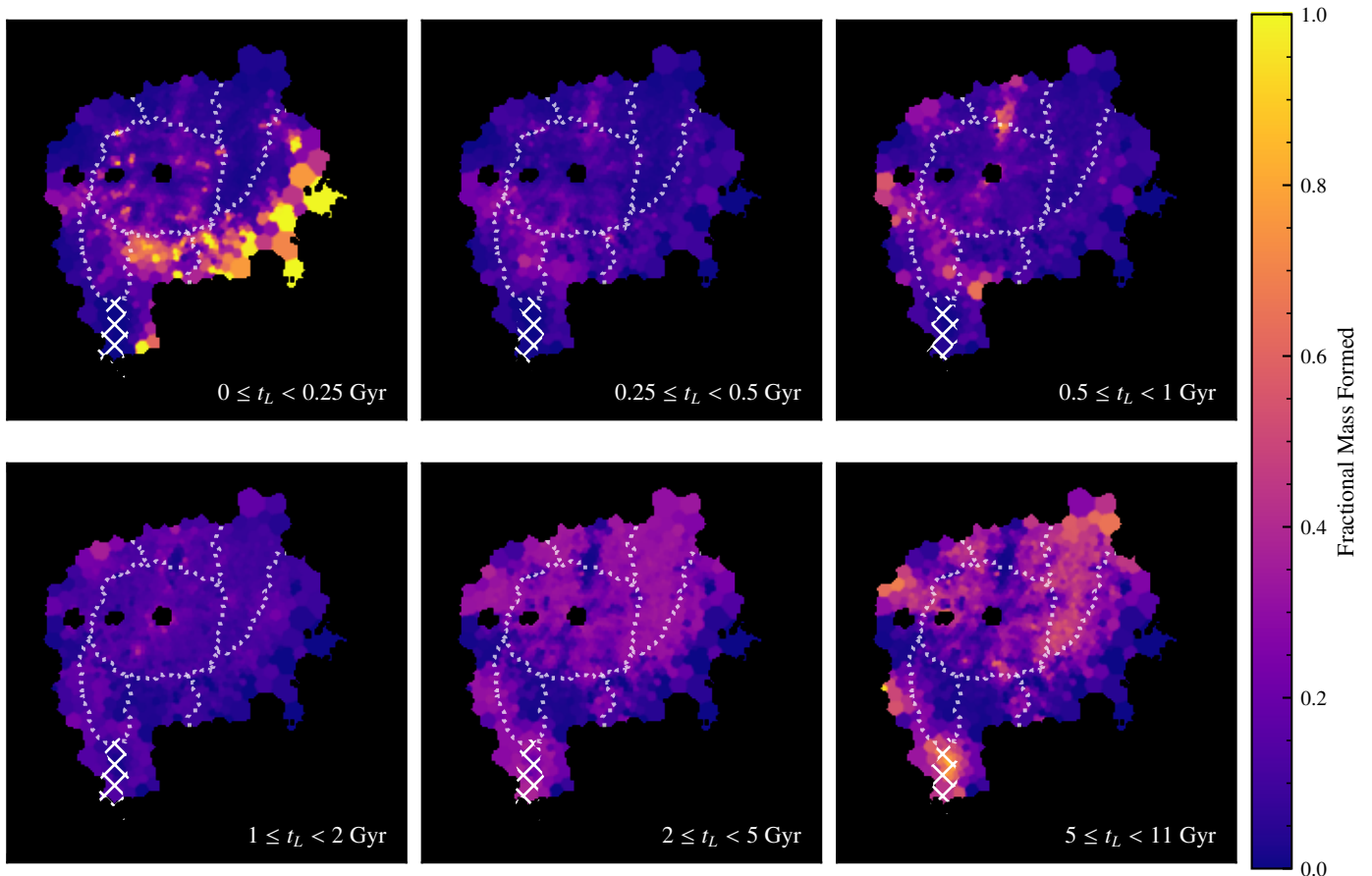


**Fig. 7.** We display here the fraction of the total stellar mass formed within different epochs, for each Voronoi bin. For ease of viewing, we have summed over the four most recent (0-0.25 Gyr) and the two oldest (5-10 Gyr) temporal bins. The dotted lines correspond to the different regions outlined in Fig. 6. The cross-hatched area is a separate galaxy, at the same redshift as F0083 (see Section 4.1).

- Region D is the inner area of the Eastern tidal feature. This area is much younger than the outer part, and contains just 1% of the mass of F0083. Whilst the SFR is extremely low at earlier epochs ( $< 0.02 M_{\odot} \text{ yr}^{-1}$  for  $t_L \geq 2$  Gyr), we see again the sharp increase at  $t_L \approx 1$  Gyr.
- Regions E and F are what have been visually classified as the “stripped tail”, with E indicating the area closest to the

tidal feature (regions C and D). These regions account for  $> 10\%$  of the current SFR of F0083, whilst containing  $< 5\%$  of the stellar mass. Both regions show a recently rising SFH with  $\text{SFR}_{20}/\text{SFR}_{100} > 1$ , and the resolved mass maps establish how recently the majority of mass has formed in these areas. We note that whilst region F shows a not insignificant amount of star formation in the earliest age bin, this can be



attributed to the masking procedure. Considering Fig. 7, it is clear that our mask for region A has not fully encompassed the entirety of the old stellar population in the spiral arm – or more accurately, the recently formed tail overlaps the existing stellar component along our line-of-sight.

- The central disc itself contains a number of blue star-forming regions, and is where the majority of star formation is taking place. As with regions E and F, it has a recently rising SFH (see Table 1. However, we note that there is a still faint imprint of the PSF “snowflake” pattern visible in the oldest age bin in Fig. 7, and so measurements in this region should be treated with more caution.

## 4. Discussion

As covered in the introduction, there are a variety of potential mechanisms that may act upon galaxies in a cluster environment. Amongst these, we focus on tidal interactions with nearby galaxies, ram-pressure stripping (RPS) due to infall into the cluster, and shock fronts from mergers of cluster substructures, and whether these physical mechanisms can explain the observed morphology and derived properties.

### 4.1. Unwinding and Tidal Interactions

One of the more unusual features of Figs. 6 and 7 is the extended South-Eastern component (regions C and D), speculatively identified as a tidal feature in Owers et al. (2012). It is not immediately clear how this feature connects to other components of F0083 – whether it is an extension of the Northern spiral arm (region B), or its own distinct component. High resolution JWST/NIRCam imaging favours the latter interpretation (see Fig. 1), with the feature comprised of an outer redder portion (region C), similar to parts of the spiral arms, and an inner blue component (region D). As noted in Section 3.3, the SFHs of these regions are unusual. Region C consists of a great many older stars, and the mass formed at different epochs is consistent with the Western and Northern spiral arms (regions A and B). However, approximately 1 Gyr ago, regions B, C, and D all show a sharp increase in SFR, with regions B and C declining again at  $t_L \approx 250$ -500 Gyr, whilst region D only begins to decline at  $t_L \approx 100$ -250 Gyr.

In Bellhouse et al. (2021), the authors present evidence that in certain circumstances, ram-pressure stripping can cause an “unwinding” effect, whereby the spiral structure of the gas is preserved in the stripped material. We do not find any particular evidence that this process is currently occurring in F0083, or is responsible for the observed structure evident in regions C and D. The predicted and observed RPS-induced unwinding should primarily affect the distribution of gas in a stripped galaxy, and the resulting young stellar populations. However, we see from Figs. 4a and 7 that both the observed spiral structure and extended feature contain a considerable fraction of stars older than 1 Gyr. These components have therefore either formed in situ, or have been redistributed to their present locations after formation; neither are recent structures on the expected timescales of ram-pressure stripping.

We suggest instead that the observed mass asymmetry is more reminiscent of a tidal interaction with a companion object, such as observed in the Whirlpool galaxy (see Fig. 7 of Wei et al. 2021 for an analogous plot). This would also explain the observed increase in SFR. Given the apparent clockwise rotation of F0083, an object moving past the Eastern side would interact with regions B, C and D in that order, in good agreement with the

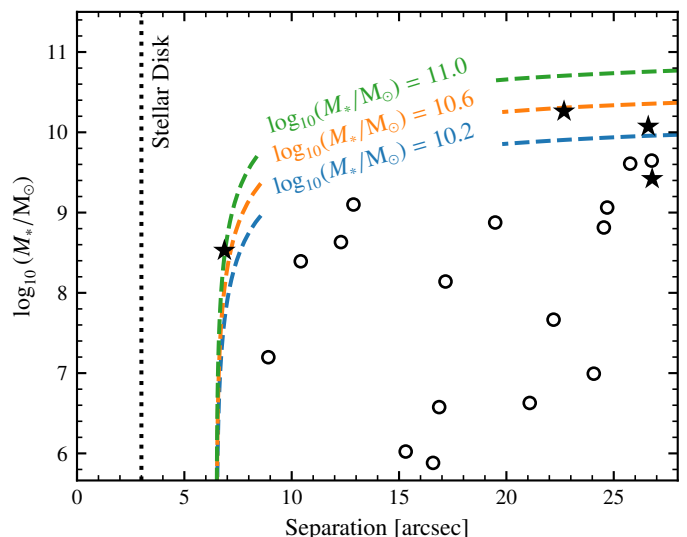


**Fig. 8.** The potential interaction candidates for F0083, displayed in the projected distance-stellar mass plane as open circles. The approximate extent of the stellar disc is shown as a dotted black line, whilst we display the selection criterion for tidal interactions as dashed lines, for a range of possible masses of F0083. Stars denote the objects which satisfy our criteria for further study.

$t_L$  of the peak SFR in each section (whether this is the *only* interaction, or simply the one which had the greatest effect on the SFR, cannot be determined from the current data). Under this assumption, it should be possible to locate the most likely interaction candidate from the surrounding field. Tidal disturbances can be parameterised by the relative ratio of the acceleration  $a_{\text{tid}}$ , produced by the neighbouring object, to  $a_{\text{gal}}$ , the acceleration produced by the potential of the galaxy of interest. From Vollmer et al. (2005), we express this ratio as

$$\frac{a_{\text{tid}}}{a_{\text{gal}}} = \frac{M_{\text{neighbour}}}{M_{\text{gal}}} \left( \frac{r}{R} - 1 \right)^{-2}, \quad (1)$$

where  $r$  is the separation between the neighbour and galaxy of interest,  $M_{\text{neighbour}}/M_{\text{gal}}$  is the total mass ratio, and  $R$  is the distance from the centre of the galaxy. Following Merluzzi et al. (2016) and Vulcani et al. (2021), we expect tidal interactions to have a significant influence on the morphology if the ratio  $a_{\text{tid}}/a_{\text{gal}} > 0.15$ . Thus, if the radial extent of the tidal stream  $R$  is known, we can estimate the required  $M_{\text{neighbour}}$  at a given distance that could be responsible.

The exact ratio detailed in Eq. 1 requires the total mass ratio and the true distance between the galaxies. As neither of these are known, we use the stellar mass ratio and projected distance as proxies, within a narrow redshift range. We search for all objects with an on-sky separation of less than  $30''$ , and with redshifts  $|z - z_{\text{F0083}}| \leq 0.01$ . We use redshifts from the MegaScience catalogues, substituting the maximum-likelihood photometric redshifts with spectroscopic measurements where available, as detailed in Section 2.4. The results are shown in Fig. 8, with 30 objects satisfying these initial criteria. We further refine our selection by estimating which objects satisfy Eq. 1 for a radius  $R = 6.5''$ , the maximum radial extent of the tidal feature (*i.e.* the outermost edge of region C). As there is some uncertainty over the true stellar mass of F0083, we select all objects satisfying the equation over a range from  $10.2 \leq \log_{10}(M_{\text{F0083}}^*/M_{\odot}) \leq 11.4$ . This leaves us with three interaction candidates. We also include a fourth galaxy (UNCOVER ID = 29959) due to its disturbed

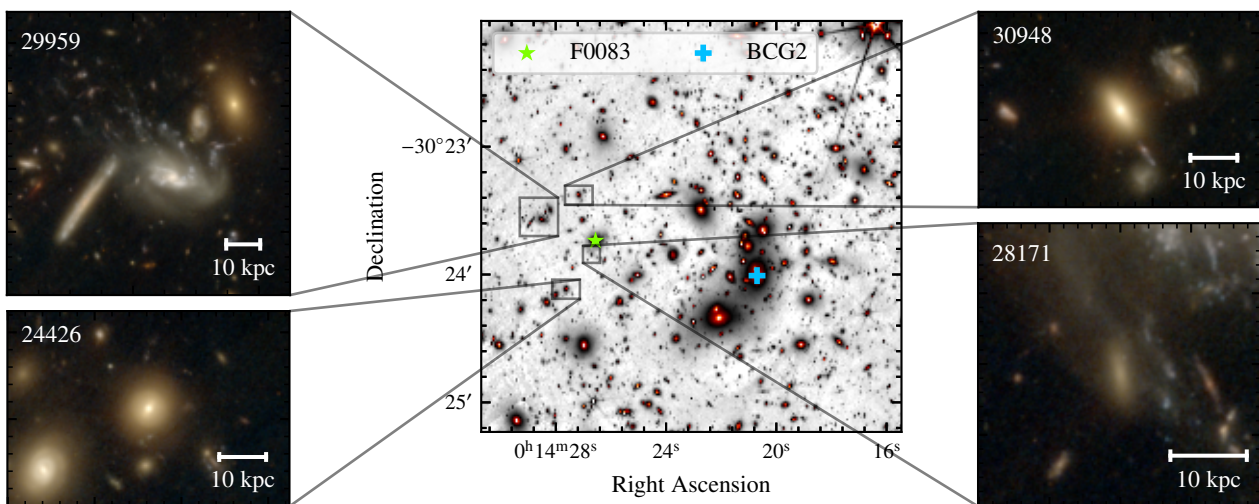


**Fig. 9.** (*centre*) The A2744 cluster field viewed through the NIRCcam F200W filter, with the location of F0083 indicated by the green star, and BCG2 the blue cross. (*outsirts*) We show RGB cutouts of the tidal interaction candidates, using the same combination of filters and image scaling as in Fig. 1.

morphology<sup>4</sup>, despite not satisfying the tidal criterion at the present epoch. We show the location and appearance of these objects in Fig. 9, their integrated star formation histories in Fig. 10, and detail their properties below. We note that there is an additional candidate galaxy, the ultra-diffuse galaxy  $\approx 8''$  West of F0083 (see Fig. 1), previously identified by Ikeda et al. (2023), with  $\log_{10}(M_*/M_\odot) \sim 7.6$ . Due to the extremely faint photometry, and lack of spectroscopic information, we do not consider the derived redshift to be accurate enough to include this galaxy at present.

#### 4.1.1. Galaxy 30948

This object is located 105 kpc North of F0083, with an estimated  $\log_{10}(M_*/M_\odot) = 10.26 \pm 0.04$ , at  $z_{\text{spec}} = 0.3026$ . From the integrated photometry, this is an entirely quiescent galaxy, with the peak SFR occurring at  $t_L \geq 5$  Gyr. As this indicates a gas-poor galaxy, it is unlikely that any recent interaction would leave a detectable signature in the photometry. Morphologically, 30948 appears to be a symmetric S0 galaxy, with no signs of any particular irregularities or disturbances. As such, we regard this as an unlikely interaction candidate.

#### 4.1.2. Galaxy 24426

This galaxy is 123 kpc South-East of F0083, at  $z_{\text{phot}} = 0.3008$ . We estimate the stellar mass to be  $\log_{10}(M_*/M_\odot) = 10.07 \pm 0.04$ , and the peak of star formation to have occurred at  $t_L \geq 7.5$  Gyr; as with 30948, this galaxy appears to be fully quenched. Visually, 24426 appears to be a barred S0 galaxy, again with no obvious asymmetry or disturbances. As with 30948, whilst we cannot definitively rule out a previous interaction with F0083, we highlight that 24426 is very close in projection and photometric redshift to two additional galaxies, a barred spiral and another barred S0 (UNCOVER IDs 24424 and 23405 respectively). We therefore consider it far more likely to have interacted with either of these galaxies, than F0083.

<sup>4</sup> This galaxy is also one of the jellyfish candidates listed by Rawle et al. (2014), named HLS001428-302334, although it was not fully covered by the HST/ACS imaging at the time.

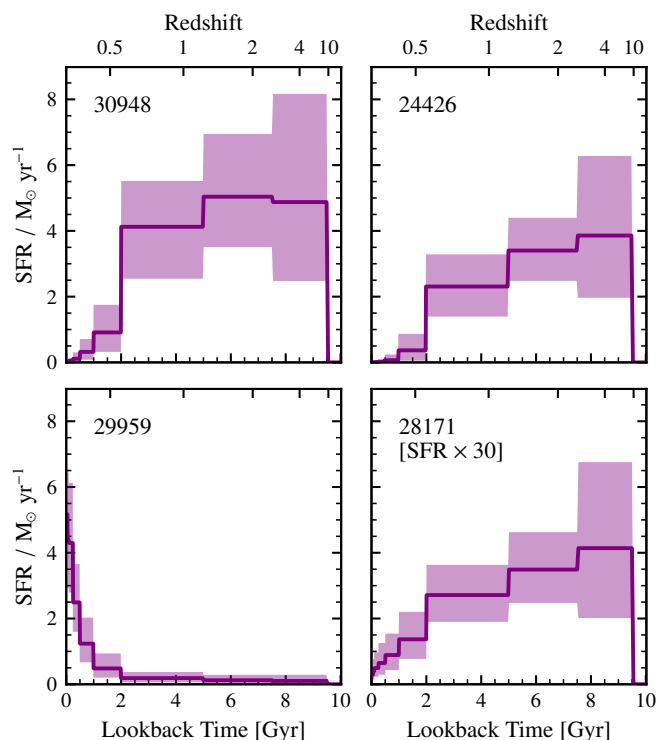


**Fig. 10.** The star formation histories of the candidate galaxies for interactions with F0083, measured from the integrated fluxes using BAGPIPES with the same method as in Section 2.5. Note that the SFR for 28171 has been multiplied by a factor of 30, in order to maintain the same y-axis scale.

#### 4.1.3. Galaxy 29959

This galaxy is located 125 kpc North-East of F0083, at  $z_{\text{spec}} = 0.3019$ , with a mass  $\log_{10}(M_*/M_\odot) = 9.42 \pm 0.07$ . It has previously been identified as a probable ram-pressure stripped galaxy by Rawle et al. (2014), based on partial HST/ACS imaging, and named HLS001428-302334. With the current JWST/NIRCAM imaging, it is clear that this galaxy has a highly disturbed morphology, with an extended tail of material stretching  $\approx 20$  kpc

towards the North-East, away from the cluster core. The nearby edge-on disc, elliptical, and irregular galaxies are merely coincident on the sky, and are all located at substantially different redshifts ( $\Delta z_{\text{phot}} > 0.05$ ). Due to the large spatial extent of this object, we opt to also derive the SFH in a spatially-resolved manner, using the same method detailed in Section 2.5, and displayed in Appendix D.

Based on the integrated SED fit shown in Fig. 10, there appears to be no particular discontinuity in the SFH, with 29959 having a continuously rising SFR. The spatially-resolved fit supports this, with 29959 showing an enhanced SFR in the tail and core, but otherwise being an excellent example of outside-in quenching, with the mass-weighted age increasing towards the edges of the galaxy. Taken together, these properties are highly suggestive of ram-pressure stripping (Gullieuszik et al. 2017). Given the large projected distance, high likelihood of RPS, and that the selection criterion for tidal interaction requires an improbably low mass for F0083 (see Fig. 8), we consider it extremely unlikely that the tidal feature in F0083 has any relation to 29959.

#### 4.1.4. Galaxy 28171

This galaxy is embedded within the tidal feature itself, at a projected distance of 31.8 kpc South-East of the core of F0083, and is also visible in both Figs. 1 and Fig. 6. From the integrated photometry, we estimate a stellar mass of  $\log_{10}(M_*/M_{\odot}) = 8.53 \pm 0.04$ , giving a comparable mass surface density to F0083 ( $\log \Sigma_*^{\text{F0083}} = 8.63$ ,  $\log \Sigma_*^{28171} = 8.62$ ). The integrated SFH presented in Fig. 10 shows a monotonically declining SFR from the earliest age bin, although at a much lower level than the other galaxies considered. Similarly, the spatially resolved stellar mass fraction shown in the hatched region of Fig. 7 seems to indicate an inside-out quenching scenario, with the galaxy almost fully quiescent at the present epoch. For both of these figures, we caution that the SFR derived near the edges of 28171 may be driven by the unavoidable flux contamination from the tidal feature itself. However, based on all of the available information, this galaxy is by far the most likely candidate for a tidal interaction with F0083.

## 4.2. Ram-Pressure Stripping

The most striking part of F0083 is the blue tail of stripped material, comprising many small knots, filaments and clumps stretching towards the South-West (regions E and F, Fig. 6). This has led to previous studies identifying F0083 as a potential ‘‘jellyfish’’, or ram-pressure stripped galaxy, primarily based on HST/ACS imaging in the F435W, F606W, and F814W bands (Owers et al. 2012; Rawle et al. 2014; Lee et al. 2022b). Compared to these studies, there is a vast increase in the amount of data available (see Appendix A for further details). One consequence is that with the expanded depth and wavelength coverage with the JWST/NIRCam imaging, it is now clear that there is a significant spatial overlap between the South-Western blue knots and filaments, and the underlying galactic disc. This link is not visible in the earlier imaging – *c.f.* Fig. 1, Fig. 2 of Owers et al. (2012). Whilst this does not change any of the overall conclusions, we posit that this may be due to ram pressure being exerted at a moderate angle with respect to the plane of the sky (see Akerman et al. 2023 for an example of the variation in gas distribution due to inclination). This inclination would account for the spectacular appearance of F0083, having both a consid-

erable number of optically bright clumps, whilst these are only a short projected distance from the galactic disc. In spectroscopic observations, this should be visible as an offset in the stellar and gas velocities. Somewhat frustratingly, the existing GMOS IFU observations of Lee et al. (2022b) have a S/N too low for reliable measurements of the stellar kinematics, and thus we conclude that this would provide an excellent opportunity for further research with deeper IFU observations.

Using the colours of the blue knots and filaments, Owers et al. (2012) estimated the upper limit on the age of these components to be  $\approx 100$  Myr. However, this is somewhat of a simplification, due to the overlap of the stellar component discussed above, and the assumption of a single stellar population. From a visual inspection of the mass maps in Fig. 7, we see that a substantial number of Voronoi bins in regions E and F formed the majority of their mass within the last 100 Myr. Importantly, there is no other epoch during which a comparable amount of mass formed. Additionally, looking at the integrated SFHs in Fig. 6, both regions see a sharp increase in SFR during the last 100 Myr, with  $\text{SFR}_{20}/\text{SFR}_{100} > 1$ . As such, we consider this result consistent with Owers et al. (2012). Within the last 100 Myr, some mechanism has triggered a sudden increase in star formation in F0083, limited only to a single side of the galaxy. The only plausible explanation is ram-pressure stripping of the gas content, resulting from either the movement of this galaxy through the ICM, or the compression of the ICM by a shock front from mergers in the cluster itself.

#### 4.2.1. Shock Fronts in the Cluster Environment

Considering the dynamics of the cluster environment discussed in Section 1.1, it is unclear precisely which mechanism may have produced the stripped tail visible in F0083. Rawle et al. (2014) suggest that the ram-pressure stripping of several galaxies, chiefly F0083 and 29959 as shown in Fig. 9, is not driven by radial infall into the cluster, due to the tails being aligned away from the cluster core. Instead, they may have been stripped by the passage of a shock front from mergers of the A2744 subclusters, which compressed the surrounding ICM. Whilst initially plausible, there are several problems with this. Firstly, for F0083, their suggested substructure passage is the interaction between the CTD and SMRC, using the terminology of Owers et al. (2011), or the Main-1 and Main-2 haloes as described by Furtak et al. (2023). However, as discussed in Section 4.2, the largely unobscured view of the star-forming knots and filaments indicate that the direction of stripping is likely occurring out of the plane of the sky. Taken with the orientation of the tail, for F0083 to be overrun with a shock front would require a merger in the NE-SW direction, towards the observer – or if F0083 were part of the merging subcluster, the reverse orientation. Neither of those scenarios has any clear observational support (see Section 1.1), and F0083 has a projected offset of  $> 400$  kpc from the closest known radio relic (Pearce et al. 2017; Rajpurohit et al. 2021).

Furthermore, we disagree with the characterisation of galaxy 29959 by Rawle et al. (2014), who suggest that the morphology and tail orientation is strongly indicative of shock-front induced RPS, similar to F0083. We concur that ram-pressure stripping is the most probable mechanism acting on this galaxy, and can rule out any ongoing interactions with F0083 (see Section 4.1.3). However, the more complete coverage of this object by JWST/NIRCam shows an extended star-forming tail pointing away from the cluster core, rather than towards the core as originally thought. Additionally, whilst there is little evidence here for the direction of stripping with respect to the line-of-sight, we

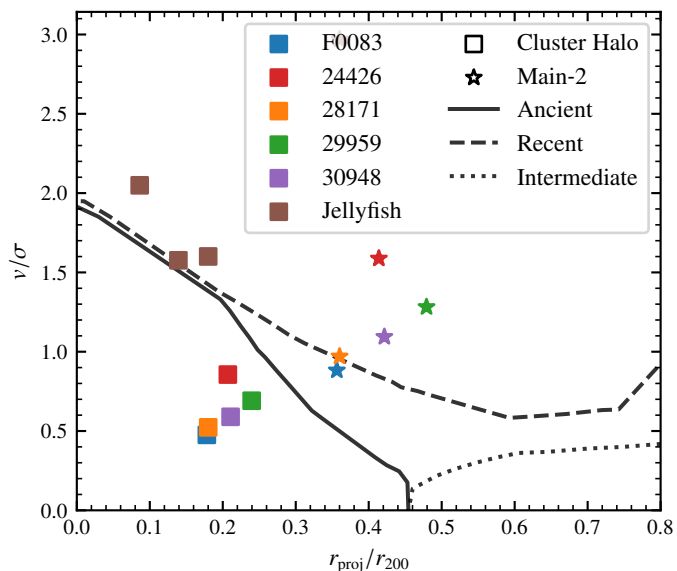


**Fig. 11.** The projected phase space diagram for Abell 2744, showing the location of F0083 and the tidal interaction candidates. The square points show the locations relative to the full cluster halo, with a virial radius of 2 Mpc and  $\sigma = 1497 \text{ km s}^{-1}$ , whereas the stars show the positions if we instead assume the Main-2 halo from Furtak et al. (2023), with  $r_{200} = 1 \text{ Mpc}$ , and  $\sigma = 807 \text{ km s}^{-1}$ . The coordinates of the halo centre are the same for both cases, R.A. = 3.58641, Dec. = -30.39997.

suggest that the observed SFH in Section 4.1.3 and Appendix D further supports this direction of stripping, in that the leading edge closest to the cluster core has a much higher  $\text{Age}_{\text{MW}}$  than the opposing edge. We conclude that there is little support from our observations of shock-front induced RPS, in this region of A2744.

#### 4.2.2. Cluster Infall

If we assume that the stripping of F0083 is solely caused by passage through the intracluster medium (ICM), it is easier to reconcile our observations with previous studies of the cluster substructure. In Fig. 11, we show the location of F0083 and the tidal interaction candidate galaxies on a projected phase-space (PPS) diagram. We also include three known jellyfish galaxies from Moretti et al. (2022) as a point of comparison, and delineate the approximate boundaries of the recent, intermediate, and ancient infalling populations, taken from Rhee et al. (2017). The position of F0083 on the PPS would seem to indicate that it is already virialised, *i.e.* not undergoing first passage, although this makes assumptions about virialisation that do not necessarily hold true for a system as complex as A2744 (Vulcani et al. 2023). However, the position here within the PPS depends entirely on the expected membership of F0083 with respect to the cluster substructures. At a redshift  $z_{\text{spec}} = 0.3033$ , F0083 is most consistent with being a member of the central substructures, likely the CTD using the formalism of Owers et al. (2011). If we eschew the overall cluster properties, and adopt instead the virial radius and velocity dispersion of the Main-2 halo of Furtak et al. (2023), the halo most consistent with the CTD substructure, F0083 lies closer to the edge of the recent ( $< 3.63 \text{ Gyr}$ ) infall region described by Rhee et al. (2017).

If F0083 is only now stripped due to first infall, we can infer the most probable formation scenario. The Main-2 halo contains BCG2, as indicated in Fig. 9. This is itself located at a redshift

$z_{\text{spec}} = 0.2997$ , from which we infer a relative peculiar velocity for F0083 of  $v_{\text{pec}} = 830 \text{ km s}^{-1}$ . Without independent distance measurements, we cannot truly separate out the cosmological redshift from the Doppler redshift due to the peculiar velocity, although this estimate is consistent with the velocity dispersion of the halo as measured from strong lensing (Furtak et al. 2023). Indeed, if F0083 were located 1 Mpc in front of or behind BCG2 (note that the projected separation is just 360 kpc), the inferred peculiar velocity would only range from  $770 - 890 \text{ km s}^{-1}$ . We rule out F0083 being located at a higher cosmological redshift, with a negative peculiar velocity – this is inconsistent with the observed morphology of the star-forming regions, as discussed in Section 4.2. We also stress that the orientation of the star-forming knots and filaments indicate a transverse velocity ( $v_{\text{trans}}$ ) component in the plane of the sky, directed away from the cluster core. The most probable scenario is thus that F0083 is approaching (or has just passed) pericentre, on an orbit around the Main-2 halo, centred on BCG2.

Whilst both pre- and post-pericentre passages are consistent with the available data, previous studies have shown that most jellyfish galaxies in clusters are stripped on first infall, with a tail visible for  $\sim 600 \text{ Myr}$  (Fumagalli et al. 2011; Roberts et al. 2021; Smith et al. 2022). This is certainly true for the most massive galaxy clusters, which contain few galaxies with high SFRs at small projected radii (Gullieuszik et al. 2020), and especially for jellyfish galaxies not undergoing edge-on stripping, the least efficient orientation for removing the gas content (Akerman et al. 2023). Although our broad-band photometric data does not allow for a derivation of the gas mass within F0083 (or the extended tail), the measurements we do have suggest substantial depletion of the gas content, fuelling extremely high SFRs, within the last 200 Myr. We therefore submit that the most probable scenario is that F0083 is approaching pericentre on its first infall.

#### 4.3. Multiple Physical Processes

In Section 4.2 we establish that F0083 appears to be undergoing ram-pressure stripping, with a sudden increase in SFR at  $t_L \lesssim 200 \text{ Myr}$ . Additionally, we show in Section 4.1 that there is considerable evidence for a tidal interaction with a compact companion object, likely 28171, within the last  $\approx 1 \text{ Gyr}$ . As discussed in Section 1, these represent clear examples of the two main subclasses of external physical processes expected to act on galaxies in dense environments. From simulations, this is not necessarily an unexpected result – Marasco et al. (2016), looking at the HI content using the EAGLE simulation, found that the most common reason for gas removal was a combination of RPS and satellite interactions<sup>5</sup>. However, observations of these processes occurring in the same galaxy are extremely rare.

This rarity stems primarily from the timescales on which these processes occur. Within a cluster, the majority of interactions are likely to be high-speed interactions (harassment, Moore et al. 1996), and thus each individual interaction takes place over a very short period of time, consistent with the simulations of Marasco et al. (2016). RPS, by contrast, may take place over a timescale of up to 3 Gyr (the exact duration depending on a vast number of variables), although the visible phase again may represent less than 600 Myr (Vulcani et al. 2022). F0083 thus represents an extremely unusual scenario – a high-mass galaxy, undergoing a low-speed minor merger/interaction ( $M_{*}^{\text{F0083}}/M_{*}^{28171} \sim 100$ ), followed by the visible phase of RPS.

<sup>5</sup> Note that “tidal interactions” within their study refers to interactions with the group or cluster halo.

## 5. Conclusion

Using deep photometric data from GLASS, UNCOVER, MegaScience, and other publicly-available surveys (Weaver et al. 2024; Suess et al. 2024, see Appendix A for details), we derive the spatially-resolved star-formation history of the galaxy F0083 using BAGPIPES, previously identified as a probable ram-pressure stripped system by Owers et al. (2012), Rawle et al. (2014), and Lee et al. (2022b). F0083 is a high-mass ( $\log_{10}(M_*/M_\odot) = 10.25 \pm 0.07$ ) spiral galaxy, with a tail of blue star-forming material extending towards the South-West from the stellar disc. The resolved star-formation rate (SFR) in this tail indicates an extremely high specific SFR over the previous 100 Myr. Additionally, the outer regions in all other quadrants show a decreasing SFR at the observed epoch, with  $\text{SFR}_{20}/\text{SFR}_{100} < 1$ . The only plausible conclusion is that F0083 is undergoing ram-pressure stripping (RPS), and we posit that the most probable scenario based on the available data is that F0083 is undergoing first infall, approaching pericentre.

F0083 also has an extended low surface brightness feature, stretching anticlockwise around the galaxy from the North to the South-East, reminiscent of the tidal features found in galaxies such as Messier 51. In Fig. 7, we show that this feature is associated with an increased SFR at  $t_L \approx 1$  Gyr, indicative of being formed by a previous interaction. We verify that both this feature and the opposing spiral arms are present in the resolved stellar mass surface density map (Fig. 4), and thus this “unwinding” effect cannot be attributed to ram-pressure stripping as in Bellhouse et al. (2021). Following the prescription of Vulcani et al. (2021), we look for all galaxies within a radius of  $30''$  ( $\sim 140$  kpc) which satisfy the equation of Vollmer et al. (2005), *i.e.* are sufficiently massive at a close enough distance to exert a tidal force on F0083. Despite the highly disturbed morphology, we find no evidence that the nearby galaxy 29959 (ID from UNCOVER DR3, also named HLS001428-302334 in Rawle et al. 2014) has previously interacted, or is sufficiently massive to currently exert a tidal force on F0083. We can confirm that 29959 appears to be undergoing outside-in quenching as a result of ram-pressure stripping, and that given the orientation of the extended tail, it is highly likely that this object is on first infall towards the cluster centre. Two other galaxies, 24426 and 30948, satisfy the tidal interaction criterion for the lower limit of  $M_*^{F0083}$ . Both appear to have S0 morphologies, and based on our SED fitting, are fully quiescent at the time of observation. Given the large projected distances, and the uncertainties over the mass of F0083, we suggest that it is unlikely that either of these galaxies are responsible for the tidal feature. Instead, we favour the compact elliptical galaxy 28171, embedded in the tidal stream along our line-of-sight as the primary cause of the disturbed morphology.

We have demonstrated that with deep photometric observations, it is possible to derive spatially-resolved star formation histories that are sufficient to constrain multiple physical processes. We hope to confirm these results with follow-up observations, and apply the method more broadly in future.

*Acknowledgements.* The data were obtained from the Mikulski Archive for Space Telescopes at the Space Telescope Science Institute, which is operated by the Association of Universities for Research in Astronomy, Inc., under NASA contract NAS 5-03127 for JWST. These observations are associated with program JWST-ERS-1324. We acknowledge financial support from NASA through grants JWST-ERS-1324. We also acknowledge support from the INAF Large Grant 2022 “Extragalactic Surveys with JWST” (PI Pentecicci). B.V. is supported by the European Union – NextGenerationEU RFF M4C2 1.1 PRIN 2022 project 2022ZSL4BL INSIGHT. MT acknowledges support by the Australian Research Council Centre of Excellence for All Sky Astrophysics in 3 Dimensions (ASTRO 3D), through project number CE170100013.

## References

- Akerman, N., Tonnesen, S., Poggianti, B. M., Smith, R., & Marasco, A. 2023, *The Astrophysical Journal*, 948, 18, publisher: IOP ADS Bibcode: 2023ApJ...948...18A
- Anderson, J. 2016, *Empirical Models for the WFC3/IR PSF*, Tech. rep., Space Telescope Science Institute, publication Title: Space Telescope WFC Instrument Science Report ADS Bibcode: 2016wfc...rept...12A
- Asplund, M., Grevesse, N., Sauval, A. J., & Scott, P. 2009, *Annual Review of Astronomy and Astrophysics*, 47, 481, aDS Bibcode: 2009ARA&A...47..481A
- Balogh, M. L., Navarro, J. F., & Morris, S. L. 2000, *The Astrophysical Journal*, 540, 113, publisher: IOP ADS Bibcode: 2000ApJ...540..113B
- Bellhouse, C., Jaffé, Y. L., Hau, G. K. T., et al. 2017, *The Astrophysical Journal*, 844, 49, publisher: IOP ADS Bibcode: 2017ApJ...844...49B
- Bellhouse, C., McGee, S. L., Smith, R., et al. 2021, *Monthly Notices of the Royal Astronomical Society*, 500, 1285, publisher: OUP ADS Bibcode: 2021MNRAS.500.1285B
- Bergamini, P., Acebron, A., Grillo, C., et al. 2023, *The Astrophysical Journal*, 952, 84, publisher: IOP ADS Bibcode: 2023ApJ...952...84B
- Bertin, E. & Arnouts, S. 1996, *Astronomy and Astrophysics Supplement Series*, 117, 393, aDS Bibcode: 1996A&AS...117..393B
- Bezanson, R., Labbe, I., Whitaker, K. E., et al. 2022, *The JWST UNCOVER Treasury survey: Ultradeep NIRSPEC and NIRCAM Observations before the Epoch of Reionization*, publication Title: arXiv e-prints ADS Bibcode: 2022arXiv221204026B
- Boschin, W., Girardi, M., Spolaor, M., & Barrena, R. 2006, *Astronomy and Astrophysics*, 449, 461, aDS Bibcode: 2006A&A...449..461B
- Boselli, A., Fossati, M., Ferrarese, L., et al. 2018, *Astronomy and Astrophysics*, 614, A56, aDS Bibcode: 2018A&A...614A..56B
- Boucaud, A., Bocchio, M., Abergel, A., et al. 2016, *Astronomy and Astrophysics*, 596, A63, aDS Bibcode: 2016A&A...596A..63B
- Brammer, G. 2019, *Astrophysics Source Code Library*, ascl:1905.001, aDS Bibcode: 2019ascl.soft05001B
- Bruzual, G. & Charlot, S. 2003, *Monthly Notices of the Royal Astronomical Society*, 344, 1000, publisher: OUP ADS Bibcode: 2003MNRAS.344.1000B
- Buchner, J., Georgakakis, A., Nandra, K., et al. 2014, *Astronomy and Astrophysics*, 564, A125, aDS Bibcode: 2014A&A...564A.125B
- Byler, N., Dalcanton, J. J., Conroy, C., & Johnson, B. D. 2017, *The Astrophysical Journal*, 840, 44, publisher: IOP ADS Bibcode: 2017ApJ...840...44B
- Byrd, G. & Valtonen, M. 1990, *The Astrophysical Journal*, 350, 89, publisher: IOP ADS Bibcode: 1990ApJ...350...89B
- Cappellari, M. & Copin, Y. 2003, *Monthly Notices of the Royal Astronomical Society*, 342, 345, publisher: OUP ADS Bibcode: 2003MNRAS.342..345C
- Cardelli, J. A., Clayton, G. C., & Mathis, J. S. 1989, *The Astrophysical Journal*, 345, 245, publisher: IOP ADS Bibcode: 1989ApJ...345..245C
- Cardoso, L. S. M., Gomes, J. M., & Papaderos, P. 2017, *Astronomy and Astrophysics*, 604, A99, aDS Bibcode: 2017A&A...604A..99C
- Carnall, A. C., McLure, R. J., Dunlop, J. S., & Davé, R. 2018, *Monthly Notices of the Royal Astronomical Society*, 480, 4379, publisher: OUP ADS Bibcode: 2018MNRAS.480.4379C
- Cha, S., HyeonHan, K., Scofield, Z. P., Joo, H., & Jee, M. J. 2024, *The Astrophysical Journal*, 961, 186, publisher: IOP ADS Bibcode: 2024ApJ...961..186C
- Chadayammuri, U., Bogdán, \., Schellenberger, G., & Zuhone, J. 2024, *Closing Pandora's Box – The deepest X-ray observations of Abell 2744 and a multi-wavelength merger picture*, publication Title: arXiv e-prints ADS Bibcode: 2024arXiv240703142C
- Ciesla, L., Charmandaris, V., Georgakakis, A., et al. 2015, *Astronomy and Astrophysics*, 576, A10, aDS Bibcode: 2015A&A...576A..10C
- Cortese, L., Catinella, B., & Smith, R. 2021, *Publications of the Astronomical Society of Australia*, 38, e035, aDS Bibcode: 2021PASA...38...35C
- Cowie, L. L. & Songaila, A. 1977, *Nature*, 266, 501, aDS Bibcode: 1977Natur.266..501C
- Dauphin, F., Anderson, J., Bajaj, V., et al. 2021, *The WFC3 and WFC3 PSF Database*, Tech. rep., Space Telescope Science Institute, publication Title: Space Telescope WFC Instrument Science Report ADS Bibcode: 2021wfc...rept...12D
- Diehl, S. & Statler, T. S. 2006, *Monthly Notices of the Royal Astronomical Society*, 368, 497, publisher: OUP ADS Bibcode: 2006MNRAS.368.497D
- Dressler, A. 1980, *The Astrophysical Journal Supplement Series*, 42, 565, publisher: IOP ADS Bibcode: 1980ApJS...42..565D
- Eskew, M., Zaritsky, D., & Meidt, S. 2012, *The Astronomical Journal*, 143, 139, publisher: IOP ADS Bibcode: 2012AJ...143..139E
- Falcón-Barroso, J., Sánchez-Blázquez, P., Vazdekis, A., et al. 2011, *Astronomy and Astrophysics*, 532, A95, aDS Bibcode: 2011A&A...532A..95F
- Ferland, G. J., Chatzikos, M., Guzmán, F., et al. 2017, *Revista Mexicana de Astronomía y Astrofísica*, 53, 385, aDS Bibcode: 2017RMxAA...53..385F
- Feroz, F., Hobson, M. P., Cameron, E., & Pettitt, A. N. 2019, *The Open Journal of Astrophysics*, 2, 10, aDS Bibcode: 2019OJAp....2E..10F

- Fritz, J., Moretti, A., Gullieuszik, M., et al. 2017, *The Astrophysical Journal*, 848, 132, publisher: IOP ADS Bibcode: 2017ApJ...848..132F
- Fumagalli, M., Gavazzi, G., Scaramella, R., & Franzetti, P. 2011, *Astronomy and Astrophysics*, 528, A46, aDS Bibcode: 2011A&A...528A..46F
- Furtak, L. J., Zitrin, A., Weaver, J. R., et al. 2023, *Monthly Notices of the Royal Astronomical Society*, 523, 4568, publisher: OUP ADS Bibcode: 2023MNRAS.523.4568F
- Gavazzi, G., Contursi, A., Carrasco, L., et al. 1995, *Astronomy and Astrophysics*, 304, 325, aDS Bibcode: 1995A&A...304..325G
- Giovannini, G., Tordi, M., & Feretti, L. 1999, *New Astronomy*, 4, 141, aDS Bibcode: 1999NewA....4..141G
- Golovich, N., Dawson, W. A., Wittman, D. M., et al. 2019, *The Astrophysical Journal*, 882, 69, publisher: IOP ADS Bibcode: 2019ApJ...882...69G
- Govoni, F., Enßlin, T. A., Feretti, L., & Giovannini, G. 2001a, *Astronomy and Astrophysics*, 369, 441, aDS Bibcode: 2001A&A...369..441G
- Govoni, F., Feretti, L., Giovannini, G., et al. 2001b, *Astronomy and Astrophysics*, 376, 803, aDS Bibcode: 2001A&A...376..803G
- Gullieuszik, M., Giunchi, E., Poggianti, B. M., et al. 2023, *The Astrophysical Journal*, 945, 54, publisher: IOP ADS Bibcode: 2023ApJ...945...54G
- Gullieuszik, M., Poggianti, B. M., McGee, S. L., et al. 2020, *The Astrophysical Journal*, 899, 13, publisher: IOP ADS Bibcode: 2020ApJ...899...13G
- Gullieuszik, M., Poggianti, B. M., Moretti, A., et al. 2017, *The Astrophysical Journal*, 846, 27, publisher: IOP ADS Bibcode: 2017ApJ...846...27G
- Gunn, J. E. & Gott, III, J. R. 1972, *The Astrophysical Journal*, 176, 1, publisher: IOP ADS Bibcode: 1972ApJ...176...1G
- Ikeda, R., Morishita, T., Tsukui, T., et al. 2023, *Monthly Notices of the Royal Astronomical Society*, 523, 6310, publisher: OUP ADS Bibcode: 2023MNRAS.523.6310I
- Jauzac, M., Eckert, D., Schwinn, J., et al. 2016, *Monthly Notices of the Royal Astronomical Society*, 463, 3876, publisher: OUP ADS Bibcode: 2016MNRAS.463.3876J
- Johnson, B. D., Leja, J., Conroy, C., & Speagle, J. S. 2021, *The Astrophysical Journal Supplement Series*, 254, 22, publisher: IOP ADS Bibcode: 2021ApJS...254...22J
- Kempner, J. C. & David, L. P. 2004, *Monthly Notices of the Royal Astronomical Society*, 349, 385, publisher: OUP ADS Bibcode: 2004MNRAS.349..385K
- Kokorev, V., Brammer, G., Fujimoto, S., et al. 2022, *The Astrophysical Journal Supplement Series*, 263, 38, publisher: IOP ADS Bibcode: 2022ApJS...263...38K
- Kroupa, P. 2001, *Monthly Notices of the Royal Astronomical Society*, 322, 231, publisher: OUP ADS Bibcode: 2001MNRAS.322..231K
- Larson, R. B., Tinsley, B. M., & Caldwell, C. N. 1980, *The Astrophysical Journal*, 237, 692, publisher: IOP ADS Bibcode: 1980ApJ...237..692L
- Lee, J. H., Lee, M. G., Mun, J. Y., Cho, B. S., & Kang, J. 2022a, *The Astrophysical Journal*, 931, L22, publisher: IOP ADS Bibcode: 2022ApJ...931L..22L
- Lee, J. H., Lee, M. G., Mun, J. Y., Cho, B. S., & Kang, J. 2022b, *The Astrophysical Journal*, 940, 24, publisher: IOP ADS Bibcode: 2022ApJ...940...24L
- Leja, J., Carnall, A. C., Johnson, B. D., Conroy, C., & Speagle, J. S. 2019, *The Astrophysical Journal*, 876, 3, publisher: IOP ADS Bibcode: 2019ApJ...876....3L
- Mahler, G., Richard, J., Clément, B., et al. 2018, *Monthly Notices of the Royal Astronomical Society*, 473, 663, publisher: OUP ADS Bibcode: 2018MNRAS.473.663M
- Marasco, A., Crain, R. A., Schaye, J., et al. 2016, *Monthly Notices of the Royal Astronomical Society*, 461, 2630, publisher: OUP ADS Bibcode: 2016MNRAS.461.2630M
- Mascia, S., Roberts-Borsani, G., Treu, T., et al. 2024, *Astronomy & Astrophysics*, publisher: EDP Sciences
- Medezinski, E., Umetsu, K., Okabe, N., et al. 2016, *The Astrophysical Journal*, 817, 24, publisher: IOP ADS Bibcode: 2016ApJ...817...24M
- Merlin, E., Santini, P., Paris, D., et al. 2024, *ASTRODEEP-JWST: NIRCам-HST multiband photometry and redshifts for half a million sources in six extragalactic deep fields*, publication Title: arXiv e-prints ADS Bibcode: 2024arXiv240900169M
- Merluzzi, P., Busarello, G., Dopita, M. A., et al. 2016, *Monthly Notices of the Royal Astronomical Society*, 460, 3345, publisher: OUP ADS Bibcode: 2016MNRAS.460.3345M
- Merritt, D. 1983, *The Astrophysical Journal*, 264, 24, publisher: IOP ADS Bibcode: 1983ApJ...264...24M
- Merten, J., Coe, D., Dupke, R., et al. 2011, *Monthly Notices of the Royal Astronomical Society*, 417, 333, publisher: OUP ADS Bibcode: 2011MNRAS.417..333M
- Moore, B., Katz, N., Lake, G., Dressler, A., & Oemler, A. 1996, *Nature*, 379, 613, aDS Bibcode: 1996Natur.379..613M
- Moretti, A., Radovich, M., Poggianti, B. M., et al. 2022, *The Astrophysical Journal*, 925, 4, publisher: IOP ADS Bibcode: 2022ApJ...925...4M
- Nulsen, P. E. J. 1982, *Monthly Notices of the Royal Astronomical Society*, 198, 1007, publisher: OUP ADS Bibcode: 1982MNRAS.198.1007N
- Oemler, Jr., A. 1974, *The Astrophysical Journal*, 194, 1, publisher: IOP ADS Bibcode: 1974ApJ...194....1O
- Owers, M. S., Couch, W. J., Nulsen, P. E. J., & Randall, S. W. 2012, *The Astrophysical Journal*, 750, L23, publisher: IOP ADS Bibcode: 2012ApJ...750L..23O
- Owers, M. S., Randall, S. W., Nulsen, P. E. J., et al. 2011, *The Astrophysical Journal*, 728, 27, publisher: IOP ADS Bibcode: 2011ApJ...728...27O
- Paris, D., Merlin, E., Fontana, A., et al. 2023, *The Astrophysical Journal*, 952, 20, publisher: IOP ADS Bibcode: 2023ApJ...952...20P
- Pearce, C. J. J., van Weeren, R. J., Andrade-Santos, F., et al. 2017, *The Astrophysical Journal*, 845, 81, publisher: IOP ADS Bibcode: 2017ApJ...845...81P
- Poggianti, B. M., Moretti, A., Gullieuszik, M., et al. 2017, *The Astrophysical Journal*, 844, 48, publisher: IOP ADS Bibcode: 2017ApJ...844...48P
- Rajpurohit, K., Vazza, F., van Weeren, R. J., et al. 2021, *Astronomy and Astrophysics*, 654, A41, aDS Bibcode: 2021A&A...654A..41R
- Rawle, T. D., Altieri, B., Egami, E., et al. 2014, *Monthly Notices of the Royal Astronomical Society*, 442, 196, publisher: OUP ADS Bibcode: 2014MNRAS.442..196R
- Renaud, F., Bournaud, F., Kraljic, K., & Duc, P. A. 2014, *Monthly Notices of the Royal Astronomical Society*, 442, L33, publisher: OUP ADS Bibcode: 2014MNRAS.442L..33R
- Rhee, J., Smith, R., Choi, H., et al. 2017, *The Astrophysical Journal*, 843, 128, publisher: IOP ADS Bibcode: 2017ApJ...843..128R
- Roberts, I. D., van Weeren, R. J., McGee, S. L., et al. 2021, *Astronomy and Astrophysics*, 652, A153, aDS Bibcode: 2021A&A...652A.153R
- Scott, T. C., Cortese, L., Brinks, E., et al. 2012, *Monthly Notices of the Royal Astronomical Society*, 419, L19, publisher: OUP ADS Bibcode: 2012MNRAS.419L..19S
- Serra, P., Oosterloo, T. A., Kamphuis, P., et al. 2024, *The MeerKAT Fornax Survey. III. Ram-pressure stripping of the tidally interacting galaxy NGC 1427A in the Fornax cluster*, publication Title: arXiv e-prints ADS Bibcode: 2024arXiv240709082S
- Smith, R., Shinn, J.-H., Tonnesen, S., et al. 2022, *The Astrophysical Journal*, 934, 86, publisher: IOP ADS Bibcode: 2022ApJ...934...86S
- Smith, R. J., Lucey, J. R., Hammer, D., et al. 2010, *Monthly Notices of the Royal Astronomical Society*, 408, 1417, publisher: OUP ADS Bibcode: 2010MNRAS.408.1417S
- Suess, K. A., Weaver, J. R., Price, S. H., et al. 2024, *Medium Bands, Mega Science: a JWST/NIRCam Medium-Band Imaging Survey of Abell 2744*, publication Title: arXiv e-prints ADS Bibcode: 2024arXiv240413132S
- Sun, M., Donahue, M., Roediger, E., et al. 2010, *The Astrophysical Journal*, 708, 946, publisher: IOP ADS Bibcode: 2010ApJ...708..946S
- Takeda, H., Nulsen, P. E. J., & Fabian, A. C. 1984, *Monthly Notices of the Royal Astronomical Society*, 298, 261, publisher: OUP ADS Bibcode: 1984MNRAS.298..261T
- Treu, T., Roberts-Borsani, G., Bradac, M., et al. 2022, *The Astrophysical Journal*, 935, 110, publisher: IOP ADS Bibcode: 2022ApJ...935..110T
- Vollmer, B., Braine, J., Combes, F., & Sofue, Y. 2005, *Astronomy and Astrophysics*, 441, 473, aDS Bibcode: 2005A&A...441..473V
- Vulcani, B., Poggianti, B. M., Moretti, A., et al. 2021, *The Astrophysical Journal*, 914, 27, publisher: IOP ADS Bibcode: 2021ApJ...914...27V
- Vulcani, B., Poggianti, B. M., Smith, R., et al. 2022, *The Astrophysical Journal*, 927, 91, publisher: IOP ADS Bibcode: 2022ApJ...927...91V
- Vulcani, B., Treu, T., Calabrò, A., et al. 2023, *The Astrophysical Journal*, 948, L15, publisher: IOP ADS Bibcode: 2023ApJ...948L..15V
- Wang, B., Leja, J., Labbé, I., et al. 2024, *The Astrophysical Journal Supplement Series*, 270, 12, publisher: IOP ADS Bibcode: 2024ApJS...270...12W
- Wang, Q. D., Owen, F., & Ledlow, M. 2004, *The Astrophysical Journal*, 611, 821, publisher: IOP ADS Bibcode: 2004ApJ...611..821W
- Weaver, J. R., Cutler, S. E., Pan, R., et al. 2024, *The Astrophysical Journal Supplement Series*, 270, 7, publisher: IOP ADS Bibcode: 2024ApJS...270....7W
- Wei, P., Zou, H., Lin, L., et al. 2021, *Research in Astronomy and Astrophysics*, 21, 006, publisher: IOP ADS Bibcode: 2021RAA...21....6W
- Werle, A., Giunchi, E., Poggianti, B., et al. 2024, *Astronomy and Astrophysics*, 682, A162, aDS Bibcode: 2024A&A...682A.162W
- Werle, A., Poggianti, B., Moretti, A., et al. 2022, *The Astrophysical Journal*, 930, 43, publisher: IOP ADS Bibcode: 2022ApJ...930...43W

## Appendix A: Observation Programmes

We show in Table ?? the details of all observational programmes contributing to the photometry used in this paper. These include all observations within  $30''$  of F0083.

## Appendix B: PSF Matching

Three of the filters to be matched to F444W are the F115W, F150W and F200W filters on JWST/NIRISS. Whilst these are in general very similar to the corresponding filters on JWST/NIRCam, we derive separate PSFs to account for the different native pixel scales of the detectors, and the pixelation effects when redrizzled to the mosaic pixel scale of  $0.04''/\text{pix}$ . For these, we directly follow the method used by Weaver et al. (2024), and select point sources based on their position in the size-magnitude plane, as traced by the ratio of fluxes within  $0.16''$  and  $0.32''$  diameter apertures, against the magnitude within the  $0.32''$  aperture. We use the default parameters of `APERPY` to generate a field-averaged PSF for each filter, rejecting sources with an AB magnitude fainter than 24, with nearby contamination, or with a cutout signal/noise (S/N) below 800. For completeness, we also derive PSFs for the F090W and F158M filters, even though the coverage in these bands does not overlap with any of the galaxies we are interested in.

For the WFC3/UVIS filters F225W, F275W, and F336W, there are no suitable unsaturated, uncontaminated point sources available in the A2744 mosaic. We therefore derive a PSF based on archival imaging. There exists already an empirical PSF model, in the `STDPSF` format (Anderson 2016); however, this covers only the central  $25 \times 25$  pixels, and not the extended diffraction spikes. Similarly, the WFC3 PSF database (Dauphin et al. 2021) offers cutouts, but extending only to a  $51 \times 51$  pixel area, significantly smaller than the  $101 \times 101$  pixel cutouts and kernels derived in Suess et al. (2024). We therefore use the PSF database to extract larger cutouts from the original images. For each filter, we select all PSFs matching the following criteria (modified from the ‘‘Good Quality PSF Subset’’ selection):

- A telescope focus between  $-2$  and  $2 \mu\text{m}$ .
- The PSF  $x$ -centre and  $y$ -centre falling between 256 and 3835 (*i.e.* not within 256 pixels of the exterior edges of the detector).
- A PSF flux between 20,000 and 90,000 electrons.
- A PSF fit quality parameter (`QFIT`) less than 0.1.
- An exposure time less than 900 seconds.
- An observation date after 9<sup>th</sup> September 2014.

Using this selection, we cutout  $201 \times 201$  pixel regions from the original `FLC` images centred on each PSF, subtracting the `MDRIZSKY` value present in the `FITS` header, and apply the same contamination rejection procedure as for the NIRISS PSFs. We relax the constraints on the S/N to allow any cutout with an integrated  $S/N > 200$ , and an AB magnitude greater than 26. This leaves us with  $\approx 200$  sources for each filter, which we stack using `APERPY` to produce an empirical detector-frame PSF. This is then reprojected to the WCS of the MegaScience mosaics, accounting for the detector distortion and orientation, and cropped to  $101 \times 101$  pixels to match the existing PSFs.

Convolution kernels for the PSFs are derived using `PYPHER` (Boucaud et al. 2016), which computes kernels using an algorithm based on Wiener filtering, without any assumptions on the spherical symmetry of the system. We set the regularisation parameter to  $3 \times 10^{-3}$ , to limit high-frequency noise, and oversample each PSF by 3x before matching, using a 3<sup>rd</sup> order spline

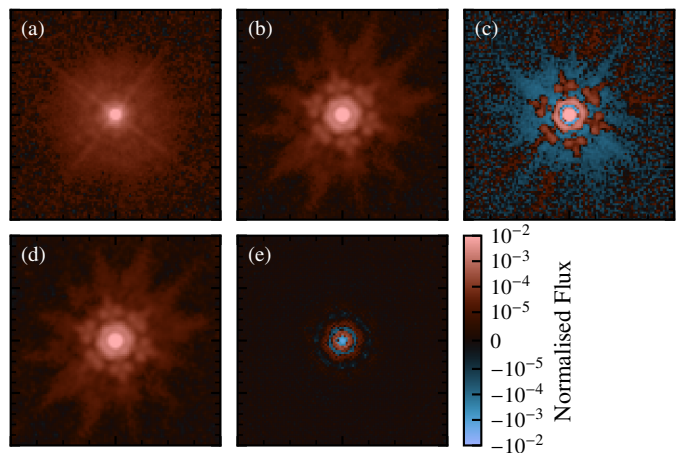


**Fig. B.1.** A visual representation of the PSF-matching procedure. All cutouts are  $2''$  per side. (a) The empirical PSF for the F275W filter in the mosaic frame, with the total flux normalised to unity. (b) The target PSF, *i.e.* the normalised F444W PSF from the MegaScience data release. (c) The convolution kernel as derived by `PYPHER`. (d) The original PSF (a) convolved with the kernel (c). (e) The residuals of the convolved PSF compared to the target, *i.e.* (d) – (b).

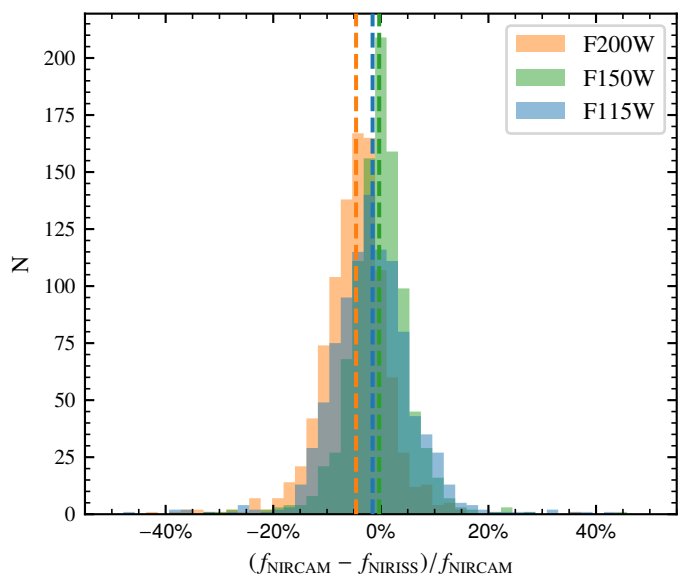


**Fig. C.1.** The relative offset between the measured fluxes in NIRCam and NIRISS in all Voronoi bins for F0083. The dashed lines show the median of the distribution for each of the three filters.

interpolation. In Fig. B.1a, we show an example of the original PSF for the F275W filter of WFC3/UVIS, compared against the target PSF in Fig. B.1b. The differences between the diffraction spikes, caused by the secondary mirror support structures, are clearly visible. In Fig. B.1c, we show the `PYPHER`-derived convolution kernel, with the convolved PSF in Fig. B.1d, and the residuals against the target in Fig. B.1e. There is still some structure visible in the residuals, most prominently in the very centre of the PSF. Whilst this fit can be improved by relaxing the regularisation parameter in `PYPHER`, doing so will also increase higher-frequency noise across the image.

## Appendix C: Photometric Uncertainties

With the exception of F158M, all filters on NIRISS originated as ‘‘flight spares’’ for NIRCam. As such, these filters are extremely

similar to their NIRCcam counterparts, and we exploit this to provide an estimate of the systematic uncertainty in the photometric measurements. At the position of F0083, only three filters have coverage in both NIRCcam and NIRISS: F115W, F150W, and F200W. In Fig. C.1, we show the relative offset between the fluxes in each instrument, for each of the three filters, as measured after convolving to a common PSF and Voronoi-binning to a S/N of 100 (see Sections 2.2 and 2.3). Typical measured uncertainties are 1.7%, 1.6% and 2.0% for F115W, F150W, and F200W respectively. We find the best agreement for F150W, with a median offset of 0.0%, and  $\sigma = 4.6\%$ . F115W shows the largest spread, with  $\sigma = 6.3\%$ , and a small offset of  $-1.5\%$  (*i.e.* the measured flux is greater in NIRISS than NIRCcam). F200W has a standard deviation of 5.1%, but a clear systematic offset of  $-4.3\%$ . As such, we consider an additional uncertainty of 5% sufficient to account for these variations.

#### Appendix D: Spatially-Resolved Properties of Galaxy 29959

We present in Fig. D.1 some of the spatially-resolved properties of the galaxy 29959. The binning procedure and SED fitting were carried out in the same manner as for F0083 in the main analysis. This leads to a small discontinuity in the tail in the maps of 29959, as the S/N in this location in the F150W filter was too low to isolate the object of interest. As discussed in Section 4.1.3, 29959 shows clear signs of outside-in quenching, with the centre still actively star-forming in Fig. D.1b, and  $\text{Age}_{\text{MW}}$  increasing with increasing radius. This latter effect is not symmetric however – the leading edge of 29959 (closest to the cluster centre) is substantially older than the trailing edge, particularly the extended tail. We posit that this is a clear indicator of ram-pressure stripping.

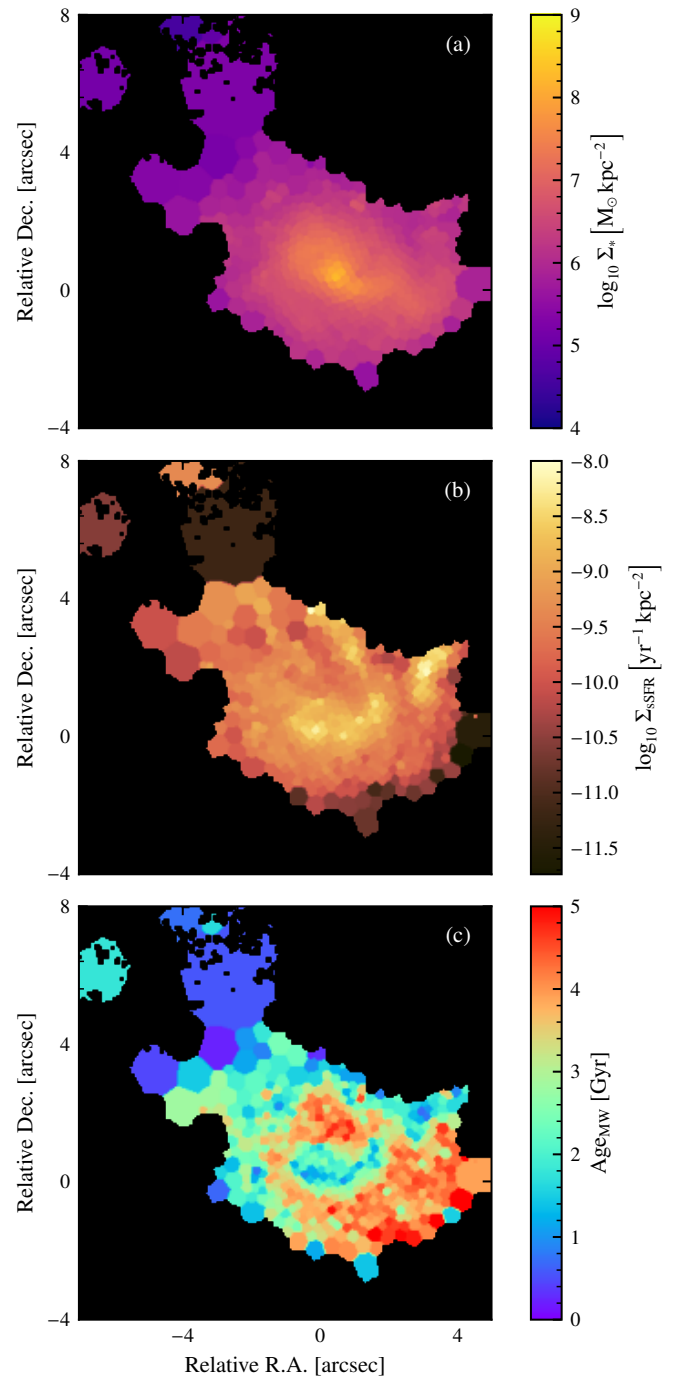


**Fig. D.1.** (a) The spatially-resolved map of the stellar mass surface density for 29959, with all external objects masked out. The discontinuity in the tail is due to the very low S/N in this area. (b) The specific star-formation rate density. Note that the lower limit of the colourmap differs from Fig. 5, in order to preserve as much detail as possible. (c) The mass-weighted age,  $\text{Age}_{\text{MW}}$ , expressed on a linear scale in Gyr.